Stem Cell Reports
Article

ISSCR

OPEN ACCESS

Loss of *Asxl1* Alters Self-Renewal and Cell Fate of Bone Marrow Stromal Cell, Leading to Bohring-Opitz-like Syndrome in Mice

Peng Zhang,[1,8] Caihong Xing,[2,3,8] Steven D. Rhodes,[4] Yongzheng He,[4] Kai Deng,[1,9] Zhaomin Li,[1] Fuhong He,[2] Caiying Zhu,[2,5] Lihn Nguyen,[4] Yuan Zhou,[5] Shi Chen,[1] Khalid S. Mohammad,[6] Theresa A. Guise,[6] Omar Abdel-Wahab,[7] Mingjiang Xu,[1] Qian-Fei Wang,[2,*] and Feng-Chun Yang[1,*]

[1]Department of Biochemistry and Molecular Biology, Sylvester Comprehensive Cancer Center, University of Miami Miller School of Medicine, Miami, FL 33136, USA
[2]Key Laboratory of Genomic and Precision Medicine, Collaborative Innovation Center of Genetics and Development, Beijing Institute of Genomics, Chinese Academy of Sciences, Beijing 100101, China
[3]Key Laboratory of Chemical Safety and Health, National Institute for Occupational Health and Poison Control, Chinese Center for Disease Control and Prevention, Beijing 100050, China
[4]Herman B. Wells Center for Pediatric Research, Indiana University School of Medicine, Indianapolis, IN 46202, USA
[5]State Key Laboratory of Experimental Hematology, Institute of Hematology and Blood Diseases Hospital and Center for Stem Cell Medicine, Chinese Academy of Medical Sciences and Peking Union Medical College, Tianjin 300020, China
[6]Department of Medicine, Indiana University School of Medicine, Indianapolis, IN 46202, USA
[7]Human Oncology and Pathogenesis Program, Memorial Sloan Kettering Cancer Center, New York, NY 10065, USA
[8]Co-first author
[9]Present address: Department of Orthopedics, The Second Hospital of Hebei Medical University, Shijiazhuang, Hebei 050000, China
*Correspondence: wangqf@big.ac.cn (Q.-F.W.), fxy37@med.miami.edu (F.-C.Y.)
http://dx.doi.org/10.1016/j.stemcr.2016.04.013

SUMMARY

De novo *ASXL1* mutations are found in patients with Bohring-Opitz syndrome, a disease with severe developmental defects and early childhood mortality. The underlying pathologic mechanisms remain largely unknown. Using *Asxl1*-targeted murine models, we found that *Asxl1* global loss as well as conditional deletion in osteoblasts and their progenitors led to significant bone loss and a markedly decreased number of bone marrow stromal cells (BMSCs) compared with wild-type littermates. $Asxl1^{-/-}$ BMSCs displayed impaired self-renewal and skewed differentiation, away from osteoblasts and favoring adipocytes. RNA-sequencing analysis revealed altered expression of genes involved in cell proliferation, skeletal development, and morphogenesis. Furthermore, gene set enrichment analysis showed decreased expression of stem cell self-renewal gene signature, suggesting a role of *Asxl1* in regulating the stemness of BMSCs. Importantly, re-introduction of *Asxl1* normalized NANOG and OCT4 expression and restored the self-renewal capacity of $Asxl1^{-/-}$ BMSCs. Our study unveils a pivotal role of ASXL1 in the maintenance of BMSC functions and skeletal development.

INTRODUCTION

Bone marrow stromal cells (BMSCs) are multi-potent progenitor cells with self-renewal capabilities and multi-lineage differentiation potentials, including osteogenesis and adipogenesis (Bianco et al., 2008; Teitelbaum, 2010; Uccelli et al., 2008; Ye et al., 2012). The relation between osteogenesis and adipogenesis in BMSCs is critical for normal bone homeostasis. Skewed cell fate of BMSCs can lead to developmental defects. For example, inhibition of adipogenesis may enhance bone growth and repair (Kawai and Rosen, 2010; McCauley, 2010). More recently, Mendez-Ferrer and others reported that the final cell-fate decision of BMSCs relies on an orchestrated activation of lineage-specific genes and repression of genes governing cell stemness or commitment to other lineages (Mendez-Ferrer et al., 2010; Takada et al., 2009; Wei et al., 2011).

Bohring-Opitz syndrome (BOS) is a heterogeneous genetic condition characterized by severe developmental delay, characteristic craniofacial appearance, fixed contractures of the upper limbs, abnormal posture, feeding difficulties, severe intellectual disability, fetal microsomia, and failure to thrive (Bohring et al., 2006; Hastings et al., 2011; Oberklaid and Danks, 1975). Most patients die in early childhood due to developmental deficits, unexplained bradycardia, obstructive apnea, or pulmonary infections (Hastings et al., 2011). In 2011, Hoischen et al. (2011) identified de novo nonsense mutations of the additional sex combs-like 1 gene (*ASXL1*) in patients with BOS. Somatic *ASXL1* alterations have also been reported in elderly patients with myeloid malignancies, including myelodysplastic syndrome, chronic myelomonocytic leukemia, and acute myeloid leukemia (Carbuccia et al., 2009; Gelsi-Boyer et al., 2009).

ASXL1 belongs to the enhancer of trithorax group (TrxG) and polycomb group (PcG) (ETP), and genetically interacts with CBX2 in mice (Fisher et al., 2010). PcG and trxG proteins are key regulators for the expression of numerous developmental genes by silencing or activating gene expression, respectively. The ETP genes encode proteins required for both maintenance of activation and silencing, as shown by simultaneous anterior and posterior transformations caused by failure to activate

or repress *Hox* genes. In an *Asxl1* mutant mouse model, Fisher et al. (2010) reported an alteration of the axial skeleton in newborn pups involving anterior and posterior transformations. However, the cellular and molecular mechanisms by which *ASXL1* mutation causes BOS remain unclear.

We have recently reported that *Asxl1* null mice are smaller in size and exhibit anophthalmia (Wang et al., 2014). In this study, we aimed to unveil the cellular and molecular mechanisms underlying the pathogenesis of *ASXL1* loss-mediated skeletal defects. Our study demonstrated that nullizygous loss of *Asxl1* led to multiple skeletal developmental defects, including runting, markedly reduced bone mineral density (BMD), microcephaly, and hypoplastic supraorbital ridges, closely reminiscent of BOS. We further identified that the defective skeletal development was associated with an impaired self-renewal and skewed lineage commitment of BMSCs, away from osteoblast and favoring adipocyte differentiation. Moreover, RNA-sequencing (RNA-seq) analysis demonstrated that *Asxl1* loss altered the expression of genes that are critical for stem cell self-renewal. Importantly, re-introduction of *Asxl1* into *Asxl1*$^{-/-}$ BMSCs restored BMSC self-renewal and lineage commitment. These data indicate a pivotal role of ASXL1 in the maintenance of BMSC functions and skeletal development.

RESULTS

Loss of *Asxl1* Impairs BMSC Self-Renewal and Differentiation Capacity

Self-renewal and multi-lineage differentiation are the two key characteristics of BMSCs. We first assessed whether *Asxl1* loss alters BMSC cellular functions. qPCR was performed to ensure that *Asxl1* was successfully deleted. While *Asxl1* mRNA was detected in wild-type (WT) BMSCs, no *Asxl1* mRNA was detected in *Asxl1*$^{-/-}$ BMSCs, indicating successful deletion of *Asxl1* (Figure S1A). *Asxl1* null mice were generated by replacing part of the *Asxl1* exon 1 sequence with *nlacZ*/*nGFP* (inserted 6 bp upstream of the start codon) as previously reported (Wang et al., 2014). The targeted allele results in transcription of *nGFP* mRNA instead of *Asxl1* (the endogenous ATG was disrupted). We examined GFP expression in the BMSCs from *Asxl1*$^{+/-}$ mice by flow-cytometric analysis to determine whether *Asxl1* is expressed in BMSCs. The CD45^{-}CD105^{+}CD44^{+} CD73^{+}CD146^{+}CD90^{+} cell population, defined as BMSCs (Barry and Murphy, 2013; Joyce and Pollard, 2009), were GFP positive (Figure S1B), suggesting expression of ASXL1 in BMSCs.

Having confirmed ASXL1 expression in WT BMSCs, we next examined the effect of *Asxl1* deletion on BMSC expansion. [^{3}H]Thymidine incorporation assays revealed that *Asxl1* ablation diminished BMSC proliferation (Figure 1A). Mendez-Ferrer et al. (2010) reported that Nestin^{+} BMSCs form non-adherent mesenspheres that can be serially replated in culture due to their self-renewal capability. We next performed clonal mesensphere cultures to determine whether loss of *Asxl1* altered BMSC self-renewal capacity. The clonal mesensphere formation potential of *Asxl1*$^{-/-}$ BMSCs was significantly reduced compared with WT BMSCs when equal numbers of BMSCs were plated (Figure 1B). WT mesenspheres were 414 ± 28.5 μm in diameter and the secondary spheres were 133 ± 20 μm in diameter (Figures 1C and 1D). In contrast, *Asxl1*$^{-/-}$ mesenspheres were significantly smaller (187.5 ± 24 μm in diameter) and exhibited a decreased capacity to form secondary spheres (64 ± 4 μm in diameter) (Figures 1C and 1D). Flow cytometric analysis revealed that the cells of the mesensphere colonies were Nestin^{+}, CD51^{+}, CD105^{+}, and CD146^{+} (Figure S1C), confirming that these cells were indeed BMSCs.

BMSCs have multi-lineage differentiation potential, including the ability to form osteoblasts and adipocytes (Pittenger et al., 1999). To evaluate the effect of *Asxl1* deletion on BMSC differentiation, we performed osteoblast and adipocyte differentiation assays. Liquid culture of BMSCs with different culture conditions verified that *Asxl1* deletion diminished osteoblast differentiation, as evidenced by minimal alkaline phosphatase-positive (ALP^{+}) expression and increased oil red O-positive ($^{+}$) cells in *Asxl1*$^{-/-}$ cultures compared with WT cultures (Figures 1E and 1F, respectively). Chondrocyte differentiation assays showed that *Asxl1* deletion did not affect chondrocyte differentiation from BMSCs (data not shown). Collectively, these data indicate that loss of *Asxl1* impairs BMSC self-renewal and skews BMSC lineage commitment away from osteoblasts but in favor of adipocytes.

Asxl1 Deletion Reduces BMSC Frequency and Alters BMSC Fates in Mice

To examine whether *Asxl1* deletion alters the BMSC frequency in vivo, we next performed flow cytometric analysis on bone marrow cells stained with a cocktail of antibodies, including CD45, CD44, CD105, CD73, CD146, and CD90 (Barry and Murphy, 2013; Joyce and Pollard, 2009). A significant reduction in the CD45^{-} CD44^{+}CD105^{+}CD73^{+}CD146^{+}CD90^{+} BMSC population was observed in the bone marrow of *Asxl1*$^{-/-}$ mice compared with WT littermates (Figure 2A). Consistently, colony-forming-unit fibroblast (CFU-F) assay, a well-established method to determine BMSC frequency in vivo, revealed a significantly reduced frequency of CFU-F in *Asxl1*$^{-/-}$ bone marrow compared with WT controls (Figures 2B and 2C). To determine whether the decreased CFU-F frequency was due solely

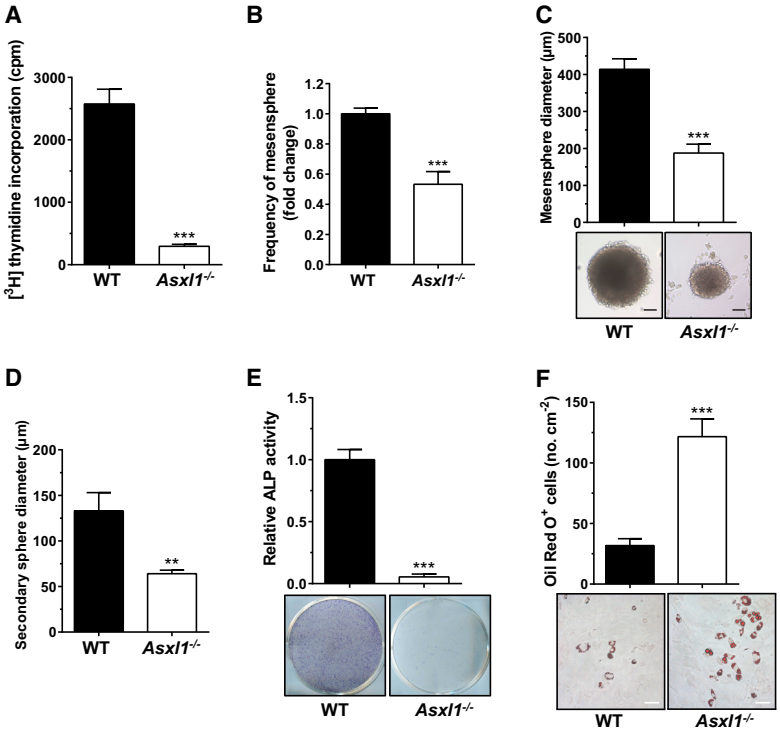

Figure 1. *Asxl1* Is Required for BMSC Self-Renewal and Differentiation

(A) Proliferation assays show impaired growth of *Asxl1*$^{-/-}$ BMSCs compared with WT (n = 4 mice per genotype from at least three independent experiments).

(B) The frequency of non-adherent mesenspheres from *Asxl1*$^{-/-}$ BMSCs is significantly decreased compared with WT BMSCs. An equal number of BMSCs were plated (n = 5 mice per genotype from three independent experiments).

(C) Self-renewal capacity of BMSCs was assayed by clonal non-adherent sphere formation. *Asxl1*$^{-/-}$ BMSCs (n = 10 mice) exhibit a significantly decreased sphere diameter compared with WT BMSCs (n = 8 mice). Scale bar represents 100 μm.

(D) The formation of secondary spheres from *Asxl1*$^{-/-}$ BMSCs is also significantly reduced compared with WT BMSCs (n = 5 mice per genotype).

(E) ALP staining shows significantly decreased osteoblast differentiation by *Asxl1*$^{-/-}$ BMSCs (n = 11 mice) as compared with WT BMSCs (n = 9 mice).

(F) Oil red O staining shows significantly increased adipocyte differentiation by *Asxl1*$^{-/-}$ BMSCs compared with WT BMSCs (n = 11 mice per genotype). Scale bar represents 50 μm.

Data are presented as mean ± SEM. **p < 0.005, ***p < 0.001. See also Figure S1.

to the decreased frequency of BMSCs in *Asxl1*$^{-/-}$ bone marrow, we performed CFU-F assays with an equal number of BMSCs. Significantly fewer CFU-F were formed by *Asxl1*$^{-/-}$ BMSCs compared with WT BMSCs (Figure S1D). These data indicate that *Asxl1* deletion decreases the BMSC pool and their CFU-F forming ability in the bone marrow in vivo.

To further evaluate the effect of *Asxl1* loss on BMSC differentiation in vivo, we subsequently performed CFU-osteoblast and CFU-adipocyte differentiation assays using primary bone marrow mononuclear cells (BMMNCs) from WT and *Asxl1*$^{-/-}$ mice. Compared with WT controls, *Asxl1*$^{-/-}$ BMMNCs gave rise to a significantly reduced number of ALP^{+} osteoblastic colonies (Figure 2D). In contrast, the total number of oil red O^{+} colonies and the ratio of oil red O^{+} colonies to CFU-F were dramatically increased in *Asxl1*$^{-/-}$ cultures (Figure 2E). Collectively, these data indicate that loss of *Asxl1* impairs BMSC self-renewal and skews BMSC lineage commitment in vivo (Figure 2F).

Genetic Deletion of *Asxl1* Leads to Multiple Skeletal Deficits Reminiscent of Human Bohring-Opitz Syndrome

Asxl1-knockout mice are smaller in size, and some mice have anophthalmia (Wang et al., 2014). Using alizarin red S/Alcian blue 8GX staining, we showed that loss of *Asxl1* resulted in ~30% reduction in body size compared with littermate controls (Figure S2A). A kinetic quantitative measurement of body size and body weight revealed significant delays in growth of *Asxl1*$^{-/-}$ mice over time compared with WT littermates (Figures S2B and S2C). *Asxl1*$^{-/-}$ mice also exhibited a significant reduction in skull size compared with their littermate controls, reminiscent of the microcephaly in BOS patients (Figure S2D). Peripheral dual-energy X-ray absorptiometry (pDEXA) revealed significantly reduced BMD in the distal femurs of *Asxl1*$^{-/-}$ mice compared with their littermate controls (Figure S2E). Microcomputed tomography (μCT) demonstrated a marked reduction of bone volume fraction in *Asxl1*$^{-/-}$ mice compared with their littermate controls (Figure S2F). Furthermore, hypoplastic supraorbital ridges, a characteristic of BOS, were observed in *Asxl1*$^{-/-}$ mice (Figure S2G).

Labeling bones with fluorochrome markers provides a method to study the dynamic changes of bone formation (Warden et al., 2005; Wu et al., 2011). We next examined bone remodeling in WT and *Asxl1*$^{-/-}$ mice with a fluorescent labeling assay. An ~45% reduction in the bone formation rate per bone surface (BFR/BS) was observed in *Asxl1*$^{-/-}$ mice compared with WT control mice (Figures S2H and S2I). These data demonstrate that loss of *Asxl1* in mice impairs skeletal development.

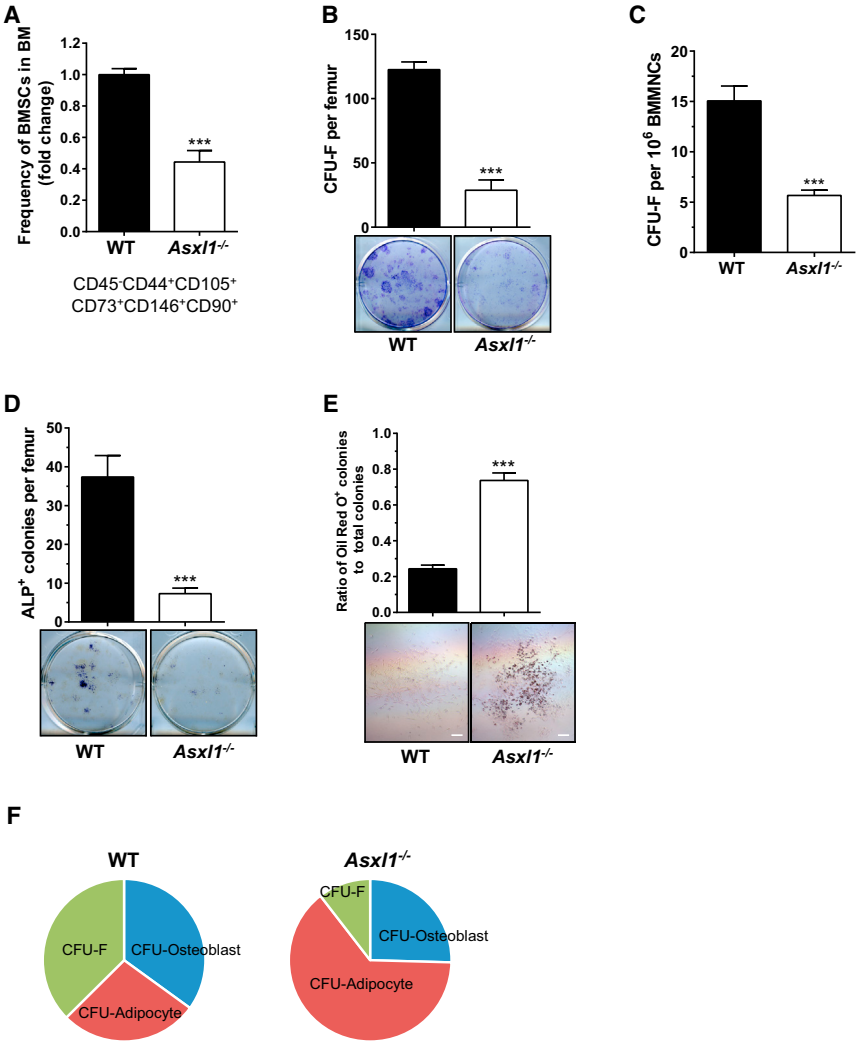

Figure 2. Loss of *Asxl1* Impairs BMSC Self-Renewal and Differentiation in Mice

(A) Quantitation of percentage of $CD45^-CD105^+CD44^+CD73^+CD146^+CD90^+$ cell populations (BMSCs) in the bone marrow of WT (n = 9 mice) and $Asxl1^{-/-}$ (n = 10 mice, 3 weeks old) by flow cytometry.

(B and C) The frequencies of CFU-F per femur (B) and per 1×10^6 BMMNCs (C) from WT and $Asxl1^{-/-}$ mice are shown (n = 6 mice per genotype).

(D) The frequencies of CFU-osteoblast (ALP^+) per femur are shown (top panel). Representative ALP staining of WT and $Asxl1^{-/-}$ osteoblastic colonies cultured in osteogenic culture medium from BMMNCs. WT (n = 8 mice) and $Asxl1^{-/-}$ (n = 7 mice).

(E) The ratio of oil red O^+ adipocytes to total colonies demonstrates enhanced adipocyte differentiation in $Asxl1^{-/-}$ BMSCs compared with WT BMSCs (n = 3 mice per genotype). Scale bar represents 200 μm.

(F) Pie chart illustrates that loss of *Asxl1* impairs BMSC self-renewal and skews BMSC lineage commitment away from osteoblasts, favoring adipocytes. Data represent the means of four independent experiments.

Data are presented as mean ± SEM. ***$p < 0.001$. See also Figure S1.

Conditional Deletion of *Asxl1* in Osteoblasts Recapitulates the Developmental Defects Observed in $Asxl1^{-/-}$ Mice

To further delineate the cell-autonomous role of ASXL1 in mediating BMSC cellular functions, we crossed *Asxl1* floxed allele mice ($Asxl1^{fl/fl}$) (Abdel-Wahab et al., 2013) with transgenic mice harboring *Osterix-Cre* (*Osx-Cre*, specifically expressed in the pre-osteoblastic and osteoblastic lineages) to generate $OsxCre;Asxl1^{fl/fl}$ mice ($OsxCre;Asxl1^{\Delta/\Delta}$) (Figure S3A). Similar to $Asxl1^{-/-}$ mice, X-ray images of $OsxCre;Asxl1^{\Delta/\Delta}$ mice at 3 weeks of age demonstrated dwarfism compared with $Asxl1^{fl/fl}$ control mice (Figure 3A). Serial measurement of body weight revealed a consistently lower body weight at varying ages of $OsxCre;Asxl1^{\Delta/\Delta}$ mice compared with age-matched littermate control mice (Figure 3B). pDEXA scans demonstrated reduced whole-body BMD and distal femoral BMD in $OsxCre;Asxl1^{\Delta/\Delta}$ mice compared with their littermate controls (Figures S3B and 3C). μCT further revealed diminished trabecular bone volume and trabecular number along with increased trabecular spacing in $OsxCre;Asxl1^{\Delta/\Delta}$ mice compared with WT controls (Figures 3D, 3E, and S3C). In addition, the cortical bone thickness of the mid-shaft femur was significantly reduced compared with control mice (Figure S3D). A greater than 50% reduction in the mineral apposition rate and a 43% reduction in the BFR/BS were observed in $OsxCre;Asxl1^{\Delta/\Delta}$ mice compared with control mice (Figures 3F and 3G). These data reinforce the cell-autonomous role of *Asxl1* deletion in defective skeletal development.

To determine whether the BMSC frequency is affected in $OsxCre;Asxl1^{\Delta/\Delta}$ mice, we examined the percentage of $PDGFR\alpha^+CD45^-TER119^-CD31^-$ BMSCs by flow cytometry (Worthley et al., 2015; Zhou et al., 2014). A significant reduction in BMSCs was observed in the bone marrow of $OsxCre;Asxl1^{\Delta/\Delta}$ mice compared with littermate controls (Figures 3H and S3E). $PDGFR\alpha^+CD45^-TER119^-CD31^-$ BMSCs from $OsxCre;Asxl1^{\Delta/\Delta}$ and controls contained a similar proportion of $Sca1^+$ and $CD51^+$ cell populations (Figure S3E). Consistently, a significant reduction in frequency of CFU-F was observed in the bone marrow of

OsxCre;Asxl1$^{\Delta/\Delta}$ mice compared with littermate control mice (Figure 3I). When plating an equal number of cells from CFU-F, we found a significant reduction of plating efficiency in *OsxCre;Asxl1*$^{\Delta/\Delta}$ BMSCs compared with control BMSCs (Figure S3F), suggesting an impaired self-renewal capacity in *OsxCre;Asxl1*$^{\Delta/\Delta}$ mice. CFU-osteoblast differentiation assays further confirmed that BMMNCs from *OsxCre;Asxl1*$^{\Delta/\Delta}$ mice gave rise to a significantly reduced number of ALP^{+} osteoblastic colonies than those of control mice (Figure 3J). The ratio of ALP^{+} osteoblast colonies to total colonies was significantly decreased in *OsxCre;Asxl1*$^{\Delta/\Delta}$ mice compared with control mice, further confirming the impaired osteoblast differentiation in *OsxCre;Asxl1*$^{\Delta/\Delta}$ mice (Figure 3K). Collectively, these data further validate our finding that loss of *Asxl1* decreases the BMSC pool and impairs osteoblast differentiation.

Asxl1 Loss Dysregulates Transcriptional Programs to Induce BMSC Lineage Commitment

To determine whether loss of *Asxl1* alters gene expression profiles in BMSCs, we next performed RNA-seq on WT and *Asxl1*$^{-/-}$ BMSCs. Compared with WT BMSCs, *Asxl1*$^{-/-}$ BMSCs exhibited a distinct gene expression signature with a total of 338 dysregulated genes. Among those, 182 genes were upregulated and 156 genes downregulated (Figure 4A). Gene ontology (GO) analysis and enrichment mapping (Merico et al., 2010; Pinto et al., 2010) demonstrated that the downregulated genes in *Asxl1*$^{-/-}$ BMSCs were enriched in skeletal development and morphogenesis (Figure 4B). Furthermore, gene set enrichment analysis (GSEA) (Subramanian et al., 2005) indicated that loss of *Asxl1* significantly decreased expression of stem cell signature genes in BMSCs (Figure 4C). By contrast, upregulated genes were enriched in cell development/differentiation and tissue morphogenesis (Figure S4).

To further validate the altered expression of key genes required for BMSC self-renewal and differentiation, we performed qPCR and western blotting with WT and *Asxl1*$^{-/-}$ BMSCs. qPCR revealed that the mRNA expression of genes critical for stem cell pluripotency, including *Nanog*, *Pou5f1*, and *Sox2*, was significantly reduced in *Asxl1* null BMSCs compared with WT BMSCs (Figure 4D), correlating with the impaired self-renewal of *Asxl1* null BMSCs. Consistently, western blot analysis revealed markedly reduced NANOG, OCT4, and SOX2 protein levels in *Asxl1* null BMSCs compared with WT cells (Figure 4E). Furthermore, mRNA expression of *Runx2*, *Sp7*, *Bglap*, and *Alpl*, genes critical for osteogenic differentiation, was also reduced in *Asxl1* null BMSCs compared with WT BMSCs (Figure 4F). By contrast, mRNA expression of *Pparγ*, *Cebpα*, *Fabp4*, and *Lpl*, genes controlling adipogenic differentiation, was dramatically increased in *Asxl1*-deficient BMSCs compared with WT BMSCs (Figure 4G). Altogether, these data suggest that ASXL1 regulates BMSC fates through controlling the expression of genes critical for BMSC self-renewal and lineage commitment.

Re-expression of *Asxl1* Rescues Self-Renewal and Osteoblast/Adipocyte Differentiation in *Asxl1*$^{-/-}$ BMSCs

To determine whether impaired self-renewal of *Asxl1*$^{-/-}$ BMSCs was a direct consequence of the *Asxl1* loss, we transduced WT *Asxl1* (with a FLAG tag for easy detection) into *Asxl1*$^{-/-}$ BMSCs using a lentiviral system. *Asxl1*$^{-/-}$ BMSCs transduced with empty vector were used as a control. The expression of ASXL1 was confirmed by western blot analysis (Figure 5A) and qPCR (Figure S5). Re-expression of WT *Asxl1* in *Asxl1*$^{-/-}$ BMSCs significantly increased mesensphere size (Figure 5B) and restored levels of NANOG and OCT4 (Figure 5C), suggesting a restoration of self-renewal capacity of *Asxl1* null BMSCs.

To determine whether re-expression of *Asxl1* could rescue the aberrant lineage commitment of *Asxl1*$^{-/-}$ BMSCs, we repeated the osteoblast and adipocyte differentiation assays. Re-expression of *Asxl1* in *Asxl1*$^{-/-}$ BMSCs increased osteoblast differentiation (Figure 5D) while inhibiting adipocyte differentiation (Figure 5E) compared with empty vector controls. qPCR confirmed that the expression levels of genes controlling osteoblast and adipocyte differentiation, including *Runx2*, *Sp7*, *Pparγ*, and *Cebpα*, were restored (Figures 5F and 5G).

DISCUSSION

De novo nonsense mutations of *ASXL1* account for approximately 75% of BOS cases (Hoischen et al., 2011; Magini et al., 2012; Russell et al., 2015). This disease is fatal, and the underlying cellular and molecular mechanisms remain unknown. Here, we report that global loss of *Asxl1* or conditional deletion in osteoblasts and their progenitors leads to multiple developmental defects, including dwarfism, hypoplastic supraorbital ridges, microcephaly, low bone mass, and growth retardation. In addition, *Asxl1* loss impairs self-renewal capacity and skews differentiation away from osteoblasts while in favor of adipocytes. Furthermore, deletion of *Asxl1* dysregulates the expression of genes controlling BMSC fates. Our study, therefore, demonstrates a pivotal role of ASXL1 in bone homeostasis.

The balance between BMSC self-renewal and differentiation is critical for skeletal homeostasis (Ito and Suda, 2014; Sambasivan and Tajbakhsh, 2007). In this study, we found that *Asxl1* null mice exhibited markedly reduced frequencies of BMSCs and CFU-F. *Asxl1* loss in BMSCs reduced mesensphere formation and diminished re-plating capability, indicating impaired BMSC self-renewal. The

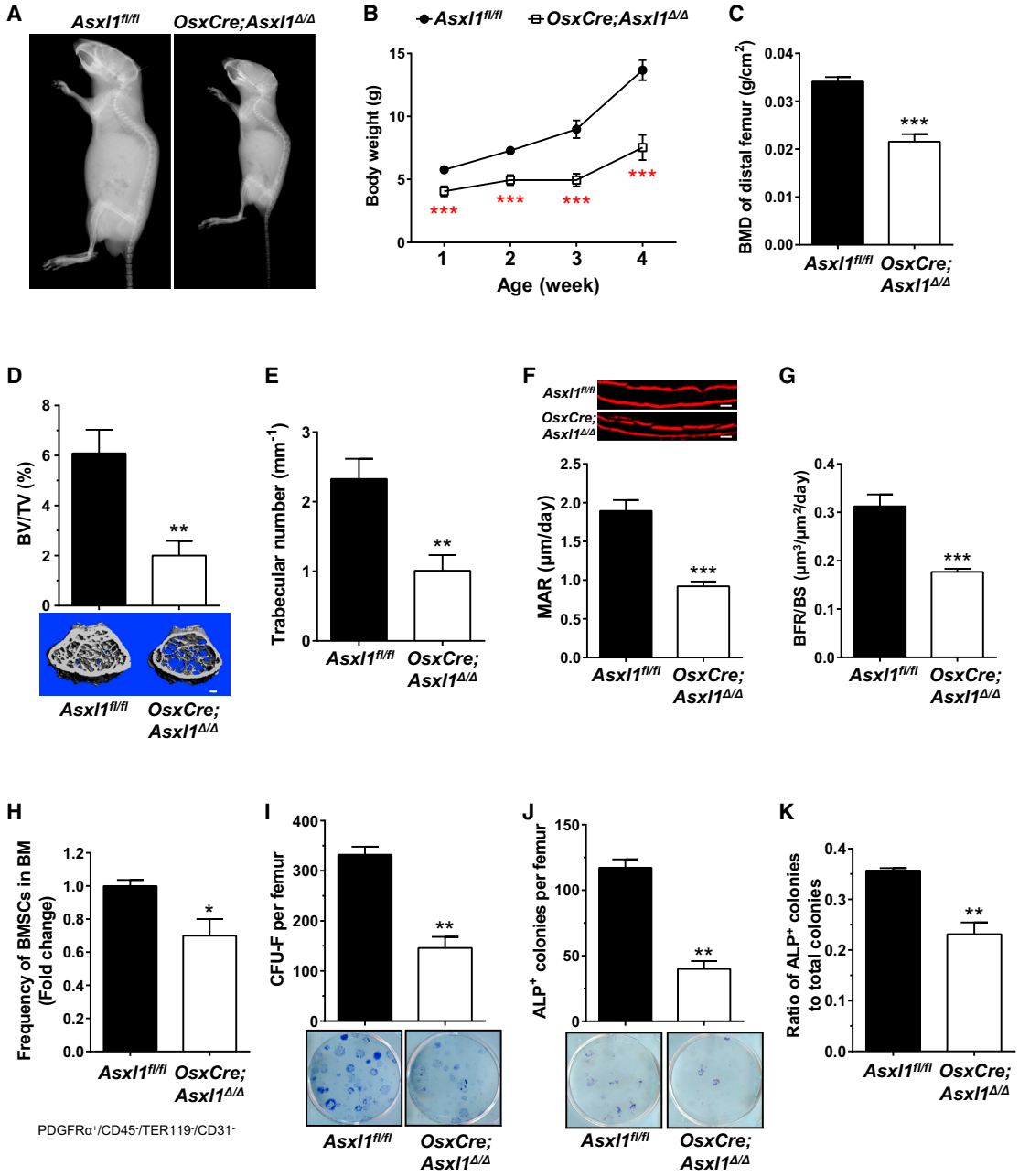

Figure 3. Loss of *Asxl1* in Pre-osteoblasts and Their Progenies Leads to BOS-like Phenotypes in Mice

(A) High-resolution X-ray images demonstrate runting of *OsxCre;Asxl1*$^{\Delta/\Delta}$ mice compared with *Asxl1*$^{fl/fl}$ littermates at 3 weeks of life.

(B) Serial body weight measurement of *OsxCre;Asxl1*$^{\Delta/\Delta}$ mice and *Asxl1*$^{fl/fl}$ littermates (n = 6 mice per genotype). Mice were weighed weekly on the same date and time.

(C) Distal femur BMD of 3-week-old *Asxl1*$^{fl/fl}$ (n = 4 mice) and *OsxCre;Asxl1*$^{\Delta/\Delta}$ (n = 6 mice).

(D and E) μCT analysis shows a significantly reduced bone volume (D) and trabecular bone (E) in *OsxCre;Asxl1*$^{\Delta/\Delta}$ (n = 6 mice) compared with *Asxl1*$^{fl/fl}$ controls (n = 4 mice). Scale bar represents 200 μm.

(F and G) Dynamic bone histomorphometry was performed using alizarin labeling. The mineral apposition rate (MAR, F) and bone formation rate (BFR/BS, G) are significantly decreased in *OsxCre;Asxl1*$^{\Delta/\Delta}$ (n = 6 mice) versus controls (n = 4 mice). Scale bar represents 20 μm.

(H) Quantitation of percentage of PDGFRα^{+}CD45^{-}TER119^{-}CD31^{-} BMSCs in the bone marrow of *OsxCre;Asxl1*$^{\Delta/\Delta}$ (n = 5 mice) and littermate controls (n = 4 mice, 5 weeks old).

(I) The frequencies of CFU-F per femur from *Asxl1*$^{fl/fl}$ (n = 5 mice) and *OsxCre;Asxl1*$^{\Delta/\Delta}$ (n = 7 mice) are shown.

(legend continued on next page)

frequency of CFU-F in *Asxl1*$^{-/-}$ bone marrow was even lower than the percentage of BMSCs as determined by flow-cytometric analysis. Thus, the dramatic reduction of CFU-F capacity of *Asxl1*$^{-/-}$ bone marrow is likely a combined effect of both reduced frequency and impaired self-renewal of BMSCs. In vitro differentiation assays also revealed markedly reduced osteoblast differentiation potential in *Asxl1*$^{-/-}$ BMSCs. In contrast, *Asxl1*$^{-/-}$ BMSCs exhibited an increased propensity for adipocyte differentiation, which is consistent with previous findings demonstrating that ASXL1 negatively regulates adipogenesis in a 3T3-L1 cell line (Park et al., 2011). These results implicate ASXL1 as a critical regulator of BMSC self-renewal and lineage commitment, providing a cellular mechanism underlying defective skeletal homeostasis associated with the *Asxl1* deletion. *ASXL1* mutations occur de novo in BOS patients, and it is therefore expected that multiple cell lineages are affected. To date, however, the specific cell lineages harboring *ASXL1* mutations in BOS patients remain unknown, and further clinical studies are warranted.

The phenotype and fate of a given cell relies on the precise control of gene expression by complex transcriptional and epigenetic networks. Such regulation of gene expression is essential for proper differentiation, cellular function, development, and homeostasis (Feng et al., 2010; Reik, 2007). Histone modifications are complex, post-translational regulatory events that play pivotal roles in governing global gene expression programs. Although extensive studies have focused on the identification of intrinsic targets of transcription factors regulating cellular fate and functions of BMSCs, the epigenetic events that control BMSC identity and/or functions remain largely unknown. In vitro studies indicate that histone modifications (including methylation and acetylation) are a key epigenetic means for gene regulation that contribute to osteogenic lineage determination (Rui et al., 2015; Tan et al., 2009).

ASXL1 regulates epigenetic marks and transcription through interaction with polycomb complex proteins and various transcription activators and repressors (Boultwood et al., 2010; Cho et al., 2006; Scheuermann et al., 2010). We and others have previously reported that loss of *Asxl1* reduces global H3K27me3 and H3K4me3 levels in myeloid progenitor cells (Abdel-Wahab et al., 2012, 2013; Wang et al., 2014). Further studies aiming to identify the chromatin and histone markers governing gene transcription for self-renewal and lineage-specific activation or repression in *Asxl1* deleted BMSCs are ongoing.

Manipulation of epigenetic mechanisms holds great promise for the future treatment of metabolic bone diseases, cancer, and a multitude of other human disease states. A better understanding of the epigenetic regulation in these processes is required for the development of potential pharmacological agents with sufficient specificity to precisely modulate chromatin remodeling on a global scale. The *Asxl1*-deficient murine model provides a compelling system to achieve such insights in the context of the human disease BOS, for which the underling molecular basis was previously unknown.

EXPERIMENTAL PROCEDURES

ASXL1 Murine Models

The generation of *Asxl1:nlacZ/nGFP* knockin and *Asxl1*$^{fl/fl}$ mice has been previously described (Abdel-Wahab et al., 2013; Wang et al., 2014). *Osx-Cre* transgenic mice were purchased from Jackson Laboratories. All mice were bred on a C57BL/6 genetic background. All protocols were approved by the Institutional Animal Care and Use Committee at University of Miami Miller School of Medicine.

BMSC Culture and Lineage Differentiation Assays

BMSCs were generated from each experimental group of mice as previously described (Wu et al., 2006). In brief, BMSCs were separated by low-density gradient centrifugation from 3- to 4-week-old mice and then resuspended and cultured in mouse MesenCult medium (MesenCult basal media plus 20% of MesenCult Supplemental; Stem Cell Technologies) at 37°C and 5% CO_2. When the cultures reached 80%–90% confluence, cells were trypsinized and re-plated. BMSCs of identical passage number (between passages 3 and 5) were used for experiments.

For osteoblast differentiation, 5 × 10^4 BMSCs were cultured for 7 days in 6-well plates using osteogenic differentiation medium (MesenCult medium supplemented with 10^{-7} M dexamethasone, 50 μg/ml ascorbic acid, and 10 mM β-glycerophosphate). For induction of adipocyte differentiation in vitro, 1 × 10^5 BMSCs were plated in 6-well tissue-culture plates and cultured with adipogenic differentiation medium (MesenCult medium supplemented with 10^{-7} M dexamethasone, 450 μM isobutylmethylxanthine, 1 μg/ml insulin, and 200 μM indomethacin). For chondrocyte differentiation assays, 1 × 10^5 BMSCs were plated in 6-well plates and cultured with chondrogenic differentiation medium (osteogenic differentiation medium supplemented with 10 ng/ml transforming growth factor β3).

Mesensphere Assays

For clonal mesensphere formation, BMSCs were plated at clonal density (~1,000 cells/cm^2) in ultralow adherent 24-well plates

(J) The frequencies of CFU osteoblasts per femur are shown (top panel). Representative ALP staining of osteoblastic colonies cultured in osteogenic culture medium from *OsxCre;Asxl1*$^{\Delta/\Delta}$ (n = 5 mice) and *Asxl1*$^{fl/fl}$ (n = 3 mice) BMMNCs.

(K) Ratio of ALP$^+$ osteoblasts to total colonies demonstrates impaired osteoblast differentiation in *OsxCre;Asxl1*$^{\Delta/\Delta}$ (n = 5 mice) compared with littermate controls (n = 3 mice).

Data are presented as mean ± SEM. *p < 0.05, **p < 0.005, ***p < 0.001. See also Figures S2 and S3.

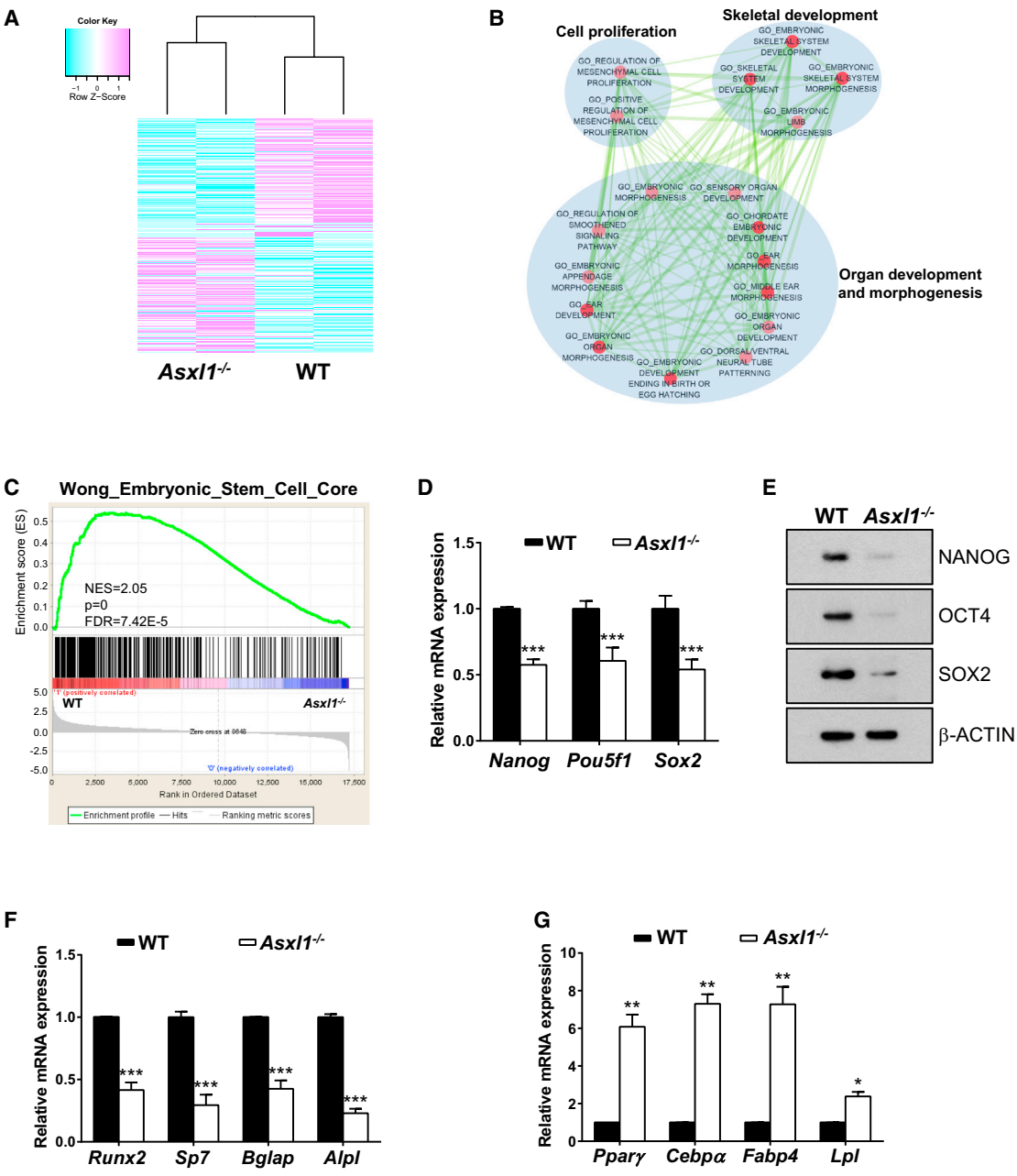

Figure 4. *Asxl1* Deletion Alters the Expression of Genes Critical for BMSCs Self-Renewal and Differentiation

(A) The heatmap shows clustering of differentially expressed genes between WT and *Asxl1*$^{-/-}$ BMSCs ($p < 0.05$, FDR < 0.25). Light purple and light blue indicate 182 up- and 156 downregulated genes, respectively.

(B) The enrichment map helps visualize the network of KEGG pathways and GO terms enriched with downregulated genes in *Asxl1*$^{-/-}$ BMSCs. Nodes and ovals indicate enriched functional gene sets ($p < 0.01$ and FDR < 0.25 in DAVID) and functional clusters, respectively. Edges indicate overlap between the enriched gene sets; thickness represents significance. Only edges with a Fisher's exact test nominal p value smaller than 10^{-4} were visualized. Color intensity is proportional to enrichment significance.

(C) The GSEA plot shows decreased gene expression of the embryonic stem cell signature (Wong et al., 2008) in *Asxl1*$^{-/-}$ BMSCs compared with WT BMSCs. The normalized enrichment score (NES), p value, and FDR are shown.

(D) qPCR analysis shows that expression levels of the pluripotent marker genes *Nanog*, *Pou5f1*, and *Sox2* are significantly lower in *Asxl1*$^{-/-}$ BMSCs than in WT BMSCs (n = 6 mice per genotype).

(E) Western blot analysis shows that the protein levels of NANOG, OCT4, and SOX2 are decreased in *Asxl1*$^{-/-}$ BMSCs compared with WT BMSCs.

(legend continued on next page)

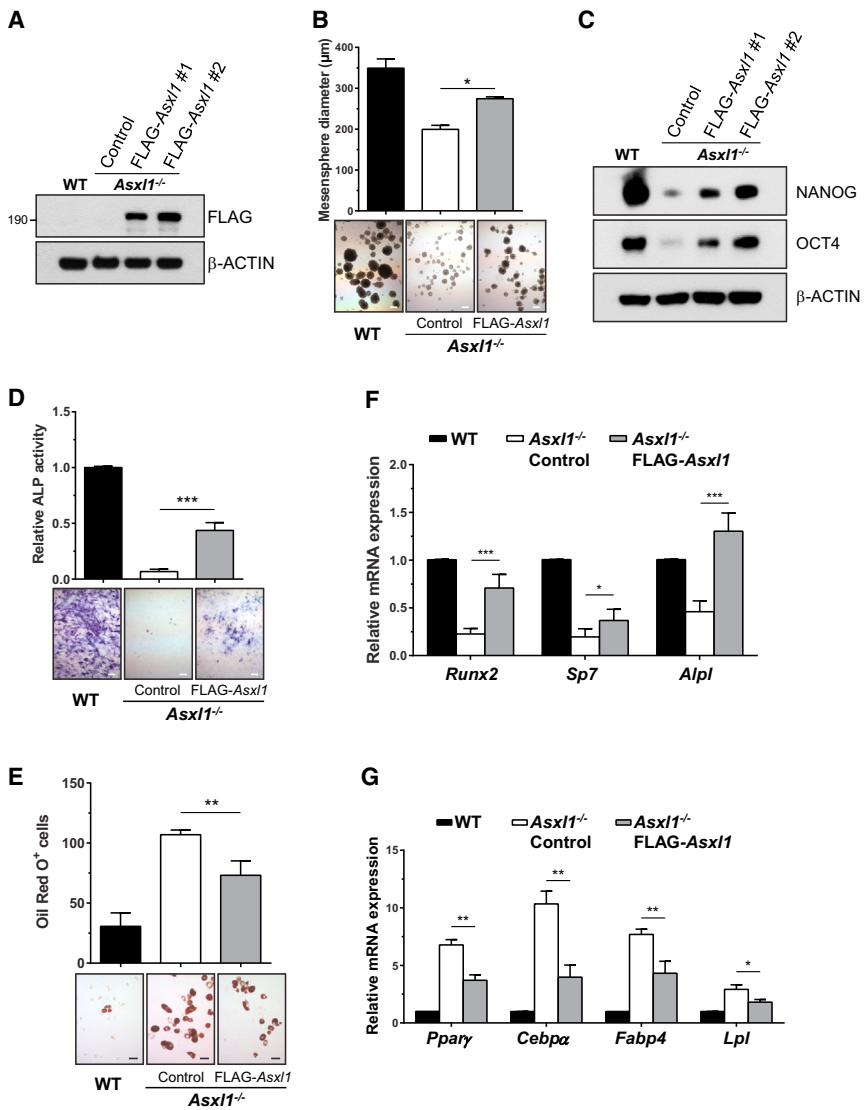

Figure 5. Re-expression of ASXL1 Rescues the Aberrant Cellular Phenotypes of *Asxl1*$^{-/-}$ BMSCs

(A) Western blot analysis shows the expression of FLAG-ASXL1 protein in *Asxl1*$^{-/-}$ BMSCs transduced with empty vector control or ASXL1 expression vector (FLAG-*Asxl1*).

(B) Mesensphere assay shows the self-renewal capacity of WT and *Asxl1*$^{-/-}$ BMSCs expressing either empty vector or FLAG-*Asxl1* as indicated. Top bars represent the mean mesensphere diameter (μm) from three independent experiments. Representative mesensphere photomicrographs are labeled accordingly. Scale bar represents 200 μm.

(C) Western blot analysis for NANOG and OCT4 in WT and *Asxl1*$^{-/-}$ BMSCs expressing either empty vector or FLAG-*Asxl1*.

(D) ALP staining of osteoblast cultures of WT BMSCs and *Asxl1*$^{-/-}$ BMSCs expressing empty vector or FLAG-*Asxl1* as indicated. Top bars represent the relative ALP^{+} activity from four independent experiments. Bottom panel shows representative photomicrographs of ALP staining cultures. Scale bar represents 200 μm.

(E) Oil red O staining of adipocyte cultures of WT or *Asxl1*$^{-/-}$ BMSCs expressing either empty vector or FLAG-*Asxl1* as indicated. Top bars represent the number of oil red O^{+} cells in cultures of WT or *Asxl1*$^{-/-}$ BMSC expressing either empty vector or FLAG-*Asxl1* from four independent experiments. Bottom panel shows representative photomicrographs of oil red O^{+} staining cells. Scale bar represents 50 μm.

(F) qPCR shows the expression of osteoblast differentiation genes (*Runx2*, *Sp7*, and *Alpl*) in WT and *Asxl1*$^{-/-}$ BMSCs transduced with FLAG-*Asxl1* or empty vector in six independent experiments.

(G) qPCR shows the expression of adipocyte differentiation genes in WT and *Asxl1*$^{-/-}$ BMSCs with or without transduction of FLAG-*Asxl1* from four independent experiments.

Data are presented as mean ± SEM. *p < 0.05, **p < 0.005, ***p < 0.001. See also Figure S5.

(Corning) as previously described (Mendez-Ferrer et al., 2010; Pinho et al., 2013). The growth medium contained 15% chicken embryo extract (Fisher Scientific), 0.1 mM β-mercaptoethanol, 1% non-essential amino acids, 1% N2 and 2% B27 supplements (Gibco), basic fibroblast growth factor, insulin-like growth factor-1, epidermal growth factor, platelet-derived growth factor, and oncostatin M (Peprotech) (20 ng/ml) in DMEM/F12 (1:1)/human endothelial (Gibco) (1:2). The cultures were maintained at 37°C in a 5% CO_2 water-jacketed incubator and left untouched for 1 week to prevent cell aggregation in low-density cultures. Half of the medium was changed weekly. The mesensphere colonies were detached with trypsin, and the cells were mechanically

(F) qPCR analysis shows decreased expression levels of the osteoblast marker genes (*Runx2*, *Bglap*, *Sp7*, and *Alpl*) in *Asxl1*$^{-/-}$ BMSCs versus WT BMSCs (n = 10 mice per genotype).

(G) qPCR analysis shows significantly increased expression of the adipocyte marker genes (*Pparγ*, *Cepbα*, *Fabp4*, and *Lpl*) in *Asxl1*$^{-/-}$ BMSCs compared with WT BMSCs (n = 4 mice per genotype).

Data are presented as mean ± SEM. *p < 0.05, **p < 0.005, ***p < 0.001. See also Figure S4.

dispersed and re-plated back into ultralow adherent plates with culture medium. Secondary mesenspheres were counted after 7 days in culture.

Generation of Stably *Asxl1*-Transduced BMSCs

The full-length mouse *Asxl1* cDNA with an N-terminal FLAG tag was cloned and then subcloned into the lentiviral vector. The empty vector was used as a control. All constructs were validated by direct sequencing prior to lentiviral generation. BMSCs were split approximately 16 hr prior to transduction and then transduced overnight with concentrated supernatants. Medium was replaced the next day, and transduced cells were cultured and expanded. $EGFP^+$ cells were sorted using a FACS Vantage flow cytometer. Before further experiments, transduction and selection efficiency were verified by qPCR and western blot analysis.

Gene Expression Analysis by qPCR and RNA-Seq

Gene of interest mRNA levels were determined by real-time qPCR. Total RNA was extracted with TRIzol reagent (Ambion). qPCR was performed in triplicate using an ABI 7500 with SYBR Green PCR kits (Applied Biosystems). mRNA levels were normalized to housekeeping gene *β-actin* expression. All qPCR primers used are listed in Table S1.

RNA-Seq reads were aligned to the mouse genome reference sequence (GRCm38/mm10) using TopHat (Trapnell et al., 2012) with a tolerance of two mismatches. Cuffdiff (Trapnell et al., 2012) was used to detect the differentially expressed genes with a cutoff of $p < 0.05$ and false discovery rate (FDR) < 0.25. The identified differentially expressed genes were used for pathway enrichment analysis and functional annotation with the Database for Annotation, Visualization and Integrated Discovery (DAVID) bioinformatics resources (Huang da et al., 2009). Heatmaps were generated in R using the gplot package. GSEA (Subramanian et al., 2005) was performed in MSigDB to generate the list of the most differentially expressed genes, including Kyoto Encyclopedia of Genes and Genomes (KEGG) pathway signatures and stem cell signatures. Enriched gene sets were selected using a cutoff of $p < 0.05$ and FDR < 0.25 (Isserlin et al., 2014).

Western Blot Analysis

BMSC cell lysates were subjected to western blot analysis. Isolated proteins were fractionated using NuPAGE 4%–12% Bis-Tris Gels (Invitrogen) and electrotransferred to polyvinylidene fluoride membranes (Roche). Immunoblots were performed using specific antibodies (Table S2). After incubation with anti-rabbit immunoglobulin G (IgG) or anti-mouse IgG (GE Healthcare) antibodies conjugated with horseradish peroxidase, signals were detected using ECL Chemiluminescence Substrate (Pierce).

Statistical Analysis

Differences between experimental groups were determined by Student's t test or ANOVA followed by Newman-Keuls multiple comparison tests as appropriate. p Values of less than 0.05 were considered significant.

ACCESSION NUMBERS

The accession number for the RNA-seq data reported in this paper is NCBI Gene Expression Omnibus GEO GSE75787 and Genome Sequence Archive (GSA) in BIG Data Center (BIGD) PRJCA000236.

SUPPLEMENTAL INFORMATION

Supplemental Information includes Supplemental Experimental Procedures, five figures, and two tables and can be found with this article online at http://dx.doi.org/10.1016/j.stemcr.2016.04.013.

AUTHOR CONTRIBUTIONS

F.-C.Y., Q.-F.W., and M.X. supervised the study; P.Z., M.X., Q.-F.W., and F.-C.Y. designed the experiments; P.Z., C.X., S.D.R., Y.H., K.D., Z.L., F.H., C.Z., L.N., Y.Z., and S.C. performed the experiments; P.Z., C.X., S.D.R., Y.H., F.H., C.Z., K.S.M., T.A.G., O.A.W., M.X., Q.-F.W., and F.-C.Y. analyzed the data; P.Z., M.X., Q.-F.W., and F.-C.Y. wrote the manuscript. All authors reviewed, edited, and approved the manuscript.

ACKNOWLEDGMENTS

This work was supported in part by grants from the NIH (CA172408 to F.-C.Y., M.X., CA185751 to F.-C.Y., M.X., and HL112294 to M.X.), the National Natural Science Foundation of China (grant 81270612 to C.X.), and the External Cooperation Program of BIC, Chinese Academy of Sciences (grant 153F11KYSB20150013 to Q.-F. W.). We thank the histological processing and analysis services provided by the Satellite Histological Core of Sylvester Comprehensive Cancer Center Core Facility.

Received: January 26, 2016
Revised: April 25, 2016
Accepted: April 26, 2016
Published: May 26, 2016

REFERENCES

Abdel-Wahab, O., Adli, M., LaFave, L.M., Gao, J., Hricik, T., Shih, A.H., Pandey, S., Patel, J.P., Chung, Y.R., Koche, R., et al. (2012). ASXL1 mutations promote myeloid transformation through loss of PRC2-mediated gene repression. Cancer Cell *22*, 180–193.

Abdel-Wahab, O., Gao, J., Adli, M., Dey, A., Trimarchi, T., Chung, Y.R., Kuscu, C., Hricik, T., Ndiaye-Lobry, D., Lafave, L.M., et al. (2013). Deletion of Asxl1 results in myelodysplasia and severe developmental defects in vivo. J. Exp. Med. *210*, 2641–2659.

Barry, F., and Murphy, M. (2013). Mesenchymal stem cells in joint disease and repair. Nat. Rev. Rheumatol. *9*, 584–594.

Bianco, P., Robey, P.G., and Simmons, P.J. (2008). Mesenchymal stem cells: revisiting history, concepts, and assays. Cell Stem Cell *2*, 313–319.

Bohring, A., Oudesluijs, G.G., Grange, D.K., Zampino, G., and Thierry, P. (2006). New cases of Bohring-Opitz syndrome, update, and critical review of the literature. Am. J. Med. Genet. A *140*, 1257–1263.

Boultwood, J., Perry, J., Pellagatti, A., Fernandez-Mercado, M., Fernandez-Santamaria, C., Calasanz, M.J., Larrayoz, M.J., Garcia-Delgado, M., Giagounidis, A., Malcovati, L., et al. (2010). Frequent mutation of the polycomb-associated gene ASXL1 in the myelodysplastic syndromes and in acute myeloid leukemia. Leukemia *24*, 1062–1065.

Carbuccia, N., Murati, A., Trouplin, V., Brecqueville, M., Adelaide, J., Rey, J., Vainchenker, W., Bernard, O.A., Chaffanet, M., Vey, N., et al. (2009). Mutations of ASXL1 gene in myeloproliferative neoplasms. Leukemia *23*, 2183–2186.

Cho, Y.S., Kim, E.J., Park, U.H., Sin, H.S., and Um, S.J. (2006). Additional sex comb-like 1 (ASXL1), in cooperation with SRC-1, acts as a ligand-dependent coactivator for retinoic acid receptor. J. Biol. Chem. *281*, 17588–17598.

Feng, S., Jacobsen, S.E., and Reik, W. (2010). Epigenetic reprogramming in plant and animal development. Science *330*, 622–627.

Fisher, C.L., Lee, I., Bloyer, S., Bozza, S., Chevalier, J., Dahl, A., Bodner, C., Helgason, C.D., Hess, J.L., Humphries, R.K., et al. (2010). Additional sex combs-like 1 belongs to the enhancer of trithorax and polycomb group and genetically interacts with Cbx2 in mice. Dev. Biol. *337*, 9–15.

Gelsi-Boyer, V., Trouplin, V., Adelaide, J., Bonansea, J., Cervera, N., Carbuccia, N., Lagarde, A., Prebet, T., Nezri, M., Sainty, D., et al. (2009). Mutations of polycomb-associated gene ASXL1 in myelodysplastic syndromes and chronic myelomonocytic leukaemia. Br. J. Haematol. *145*, 788–800.

Hastings, R., Cobben, J.M., Gillessen-Kaesbach, G., Goodship, J., Hove, H., Kjaergaard, S., Kemp, H., Kingston, H., Lunt, P., Mansour, S., et al. (2011). Bohring-Opitz (Oberklaid-Danks) syndrome: clinical study, review of the literature, and discussion of possible pathogenesis. Eur. J. Hum. Genet. *19*, 513–519.

Hoischen, A., van Bon, B.W., Rodriguez-Santiago, B., Gilissen, C., Vissers, L.E., de Vries, P., Janssen, I., van Lier, B., Hastings, R., Smithson, S.F., et al. (2011). De novo nonsense mutations in ASXL1 cause Bohring-Opitz syndrome. Nat. Genet. *43*, 729–731.

Huang da, W., Sherman, B.T., and Lempicki, R.A. (2009). Systematic and integrative analysis of large gene lists using DAVID bioinformatics resources. Nat. Protoc. *4*, 44–57.

Isserlin, R., Merico, D., Voisin, V., and Bader, G.D. (2014). Enrichment Map - a Cytoscape app to visualize and explore OMICs pathway enrichment results. F1000Res. *3*, 141.

Ito, K., and Suda, T. (2014). Metabolic requirements for the maintenance of self-renewing stem cells. Nat. Rev. Mol. Cell Biol. *15*, 243–256.

Joyce, J.A., and Pollard, J.W. (2009). Microenvironmental regulation of metastasis. Nat. Rev. Cancer *9*, 239–252.

Kawai, M., and Rosen, C.J. (2010). PPARgamma: a circadian transcription factor in adipogenesis and osteogenesis. Nat. Rev. Endocrinol. *6*, 629–636.

Magini, P., Della Monica, M., Uzielli, M.L., Mongelli, P., Scarselli, G., Gambineri, E., Scarano, G., and Seri, M. (2012). Two novel patients with Bohring-Opitz syndrome caused by de novo ASXL1 mutations. Am. J. Med. Genet. A *158A*, 917–921.

McCauley, L.K. (2010). c-Maf and you won't see fat. J. Clin. Invest. *120*, 3440–3442.

Mendez-Ferrer, S., Michurina, T.V., Ferraro, F., Mazloom, A.R., Macarthur, B.D., Lira, S.A., Scadden, D.T., Ma'ayan, A., Enikolopov, G.N., and Frenette, P.S. (2010). Mesenchymal and haematopoietic stem cells form a unique bone marrow niche. Nature *466*, 829–834.

Merico, D., Isserlin, R., Stueker, O., Emili, A., and Bader, G.D. (2010). Enrichment map: a network-based method for gene-set enrichment visualization and interpretation. PLoS One *5*, e13984.

Oberklaid, F., and Danks, D.M. (1975). The Opitz trigonocephaly syndrome. A case report. Am. J. Dis. Child. *129*, 1348–1349.

Park, U.H., Yoon, S.K., Park, T., Kim, E.J., and Um, S.J. (2011). Additional Sex Comb-like (ASXL) proteins 1 and 2 play opposite roles in adipogenesis via reciprocal regulation of peroxisome proliferator-activated receptor gamma. J. Biol. Chem. *286*, 1354–1363.

Pinho, S., Lacombe, J., Hanoun, M., Mizoguchi, T., Bruns, I., Kunisaki, Y., and Frenette, P.S. (2013). PDGFRalpha and CD51 mark human nestin+ sphere-forming mesenchymal stem cells capable of hematopoietic progenitor cell expansion. J. Exp. Med. *210*, 1351–1367.

Pinto, D., Pagnamenta, A.T., Klei, L., Anney, R., Merico, D., Regan, R., Conroy, J., Magalhaes, T.R., Correia, C., Abrahams, B.S., et al. (2010). Functional impact of global rare copy number variation in autism spectrum disorders. Nature *466*, 368–372.

Pittenger, M.F., Mackay, A.M., Beck, S.C., Jaiswal, R.K., Douglas, R., Mosca, J.D., Moorman, M.A., Simonetti, D.W., Craig, S., and Marshak, D.R. (1999). Multilineage potential of adult human mesenchymal stem cells. Science *284*, 143–147.

Reik, W. (2007). Stability and flexibility of epigenetic gene regulation in mammalian development. Nature *447*, 425–432.

Rui, Y., Xu, L., Chen, R., Zhang, T., Lin, S., Hou, Y., Liu, Y., Meng, F., Liu, Z., Ni, M., et al. (2015). Epigenetic memory gained by priming with osteogenic induction medium improves osteogenesis and other properties of mesenchymal stem cells. Sci. Rep. *5*, 11056.

Russell, B., Johnston, J.J., Biesecker, L.G., Kramer, N., Pickart, A., Rhead, W., Tan, W.H., Brownstein, C.A., Kate Clarkson, L., Dobson, A., et al. (2015). Clinical management of patients with ASXL1 mutations and Bohring-Opitz syndrome, emphasizing the need for Wilms tumor surveillance. Am. J. Med. Genet. A *167*, 2122–2131.

Sambasivan, R., and Tajbakhsh, S. (2007). Skeletal muscle stem cell birth and properties. Semin. Cell Dev. Biol. *18*, 870–882.

Scheuermann, J.C., de Ayala Alonso, A.G., Oktaba, K., Ly-Hartig, N., McGinty, R.K., Fraterman, S., Wilm, M., Muir, T.W., and Muller, J. (2010). Histone H2A deubiquitinase activity of the Polycomb repressive complex PR-DUB. Nature *465*, 243–247.

Subramanian, A., Tamayo, P., Mootha, V.K., Mukherjee, S., Ebert, B.L., Gillette, M.A., Paulovich, A., Pomeroy, S.L., Golub, T.R., Lander, E.S., et al. (2005). Gene set enrichment analysis: a knowledge-based approach for interpreting genome-wide expression profiles. Proc. Natl. Acad. Sci. USA *102*, 15545–15550.

Takada, I., Kouzmenko, A.P., and Kato, S. (2009). Wnt and PPARgamma signaling in osteoblastogenesis and adipogenesis. Nat. Rev. Rheumatol. *5*, 442–447.

Tan, J., Lu, J., Huang, W., Dong, Z., Kong, C., Li, L., Gao, L., Guo, J., and Huang, B. (2009). Genome-wide analysis of histone H3 lysine9 modifications in human mesenchymal stem cell osteogenic differentiation. PLoS One *4*, e6792.

Teitelbaum, S.L. (2010). Stem cells and osteoporosis therapy. Cell Stem Cell *7*, 553–554.

Trapnell, C., Roberts, A., Goff, L., Pertea, G., Kim, D., Kelley, D.R., Pimentel, H., Salzberg, S.L., Rinn, J.L., and Pachter, L. (2012). Differential gene and transcript expression analysis of RNA-seq experiments with TopHat and Cufflinks. Nat. Protoc. *7*, 562–578.

Uccelli, A., Moretta, L., and Pistoia, V. (2008). Mesenchymal stem cells in health and disease. Nat. Rev. Immunol. *8*, 726–736.

Wang, J., Li, Z., He, Y., Pan, F., Chen, S., Rhodes, S., Nguyen, L., Yuan, J., Jiang, L., Yang, X., et al. (2014). Loss of Asxl1 leads to myelodysplastic syndrome-like disease in mice. Blood *123*, 541–553.

Warden, S.J., Robling, A.G., Sanders, M.S., Bliziotes, M.M., and Turner, C.H. (2005). Inhibition of the serotonin (5-hydroxytryptamine) transporter reduces bone accrual during growth. Endocrinology *146*, 685–693.

Wei, Y., Chen, Y.H., Li, L.Y., Lang, J., Yeh, S.P., Shi, B., Yang, C.C., Yang, J.Y., Lin, C.Y., Lai, C.C., et al. (2011). CDK1-dependent phosphorylation of EZH2 suppresses methylation of H3K27 and promotes osteogenic differentiation of human mesenchymal stem cells. Nat. Cell Biol. *13*, 87–94.

Wong, D.J., Liu, H., Ridky, T.W., Cassarino, D., Segal, E., and Chang, H.Y. (2008). Module map of stem cell genes guides creation of epithelial cancer stem cells. Cell Stem Cell *2*, 333–344.

Worthley, D.L., Churchill, M., Compton, J.T., Tailor, Y., Rao, M., Si, Y., Levin, D., Schwartz, M.G., Uygur, A., Hayakawa, Y., et al. (2015). Gremlin 1 identifies a skeletal stem cell with bone, cartilage, and reticular stromal potential. Cell *160*, 269–284.

Wu, X., Estwick, S.A., Chen, S., Yu, M., Ming, W., Nebesio, T.D., Li, Y., Yuan, J., Kapur, R., Ingram, D., et al. (2006). Neurofibromin plays a critical role in modulating osteoblast differentiation of mesenchymal stem/progenitor cells. Hum. Mol. Genet. *15*, 2837–2845.

Wu, X., Chen, S., He, Y., Rhodes, S.D., Mohammad, K.S., Li, X., Yang, X., Jiang, L., Nalepa, G., Snider, P., et al. (2011). The haploinsufficient hematopoietic microenvironment is critical to the pathological fracture repair in murine models of neurofibromatosis type 1. PLoS One *6*, e24917.

Ye, L., Fan, Z., Yu, B., Chang, J., Al Hezaimi, K., Zhou, X., Park, N.H., and Wang, C.Y. (2012). Histone demethylases KDM4B and KDM6B promotes osteogenic differentiation of human MSCs. Cell Stem Cell *11*, 50–61.

Zhou, B.O., Yue, R., Murphy, M.M., Peyer, J.G., and Morrison, S.J. (2014). Leptin-receptor-expressing mesenchymal stromal cells represent the main source of bone formed by adult bone marrow. Cell Stem Cell *15*, 154–168.

Stem Cell Reports, Volume *6*

Supplemental Information

Loss of *Asxl1* Alters Self-Renewal and Cell Fate of Bone Marrow Stromal Cell, Leading to Bohring-Opitz-like Syndrome in Mice

Peng Zhang, Caihong Xing, Steven D. Rhodes, Yongzheng He, Kai Deng, Zhaomin Li, Fuhong He, Caiying Zhu, Lihn Nguyen, Yuan Zhou, Shi Chen, Khalid S. Mohammad, Theresa A. Guise, Omar Abdel-Wahab, Mingjiang Xu, Qian-Fei Wang, and Feng-Chun Yang

Stem Cell Reports, Volume *6*

Supplemental Information

Loss of *Asxl1* Alters Self-Renewal and Cell Fate of Bone Marrow Stromal Cell, Leading to Bohring-Opitz-like Syndrome in Mice

Peng Zhang, Caihong Xing, Steven D. Rhodes, Yongzheng He, Kai Deng, Zhaomin Li, Fuhong He, Caiying Zhu, Lihn Nguyen, Yuan Zhou, Shi Chen, Khalid S. Mohammad, Theresa A. Guise, Omar Abdel-Wahab, Mingjiang Xu, Qian-Fei Wang, and Feng-Chun Yang

Inventory of Supplemental Information

Figure S1: Linked to Figure 1 and Figure 2

Figure S2: Linked to Figure 3

Figure S3: Linked to Figure 3

Figure S4: Linked to Figure 4

Figure S5: Linked to Figure 5

Table S1 and Table S2

Supplemental Experimental Procedures

Supplemental References

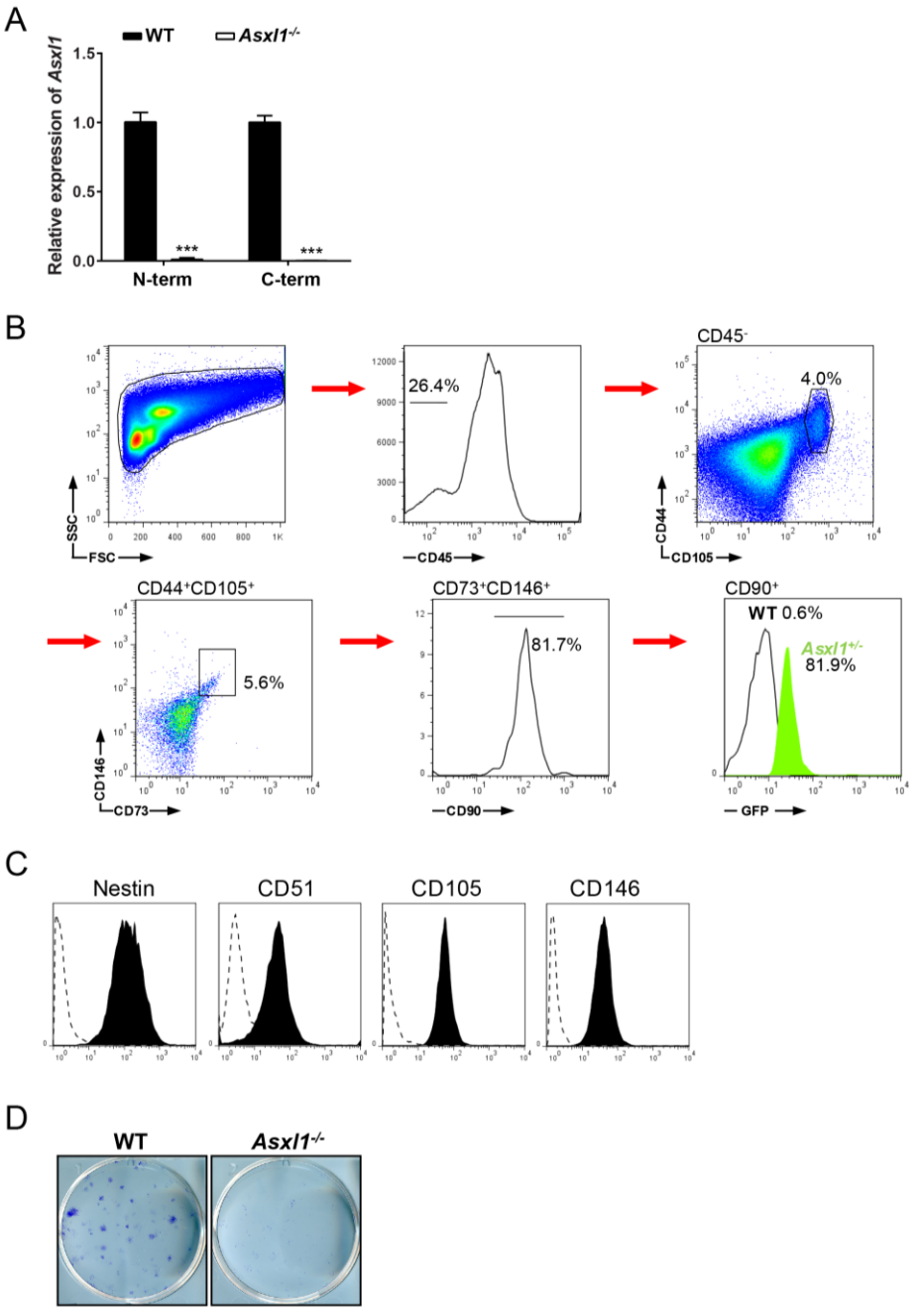

Figure S1. Related to Figure 1 and Figure 2. (A) qPCR shows the expression level of *Asxl1* in WT and *Asxl1*$^{-/-}$ BMSCs (n=7 mice per genotype). N-term and C-term indicate the position of primers used. (B) Representative flow cytometry plots show the population of BMSCs in the bone marrow of WT and *Asxl1*$^{+/-}$ mice. (C) Representative flow cytometric analysis of clonal non-adherent mesenspheres cultured from BMSCs. (D) A representative photomicrograph of CFU-F from WT and *Asxl1*$^{-/-}$ BMSCs, after staining with the HEMA-3 Quick Staining Kit.

Data are presented as mean ± SEM. ***$p < 0.001$.

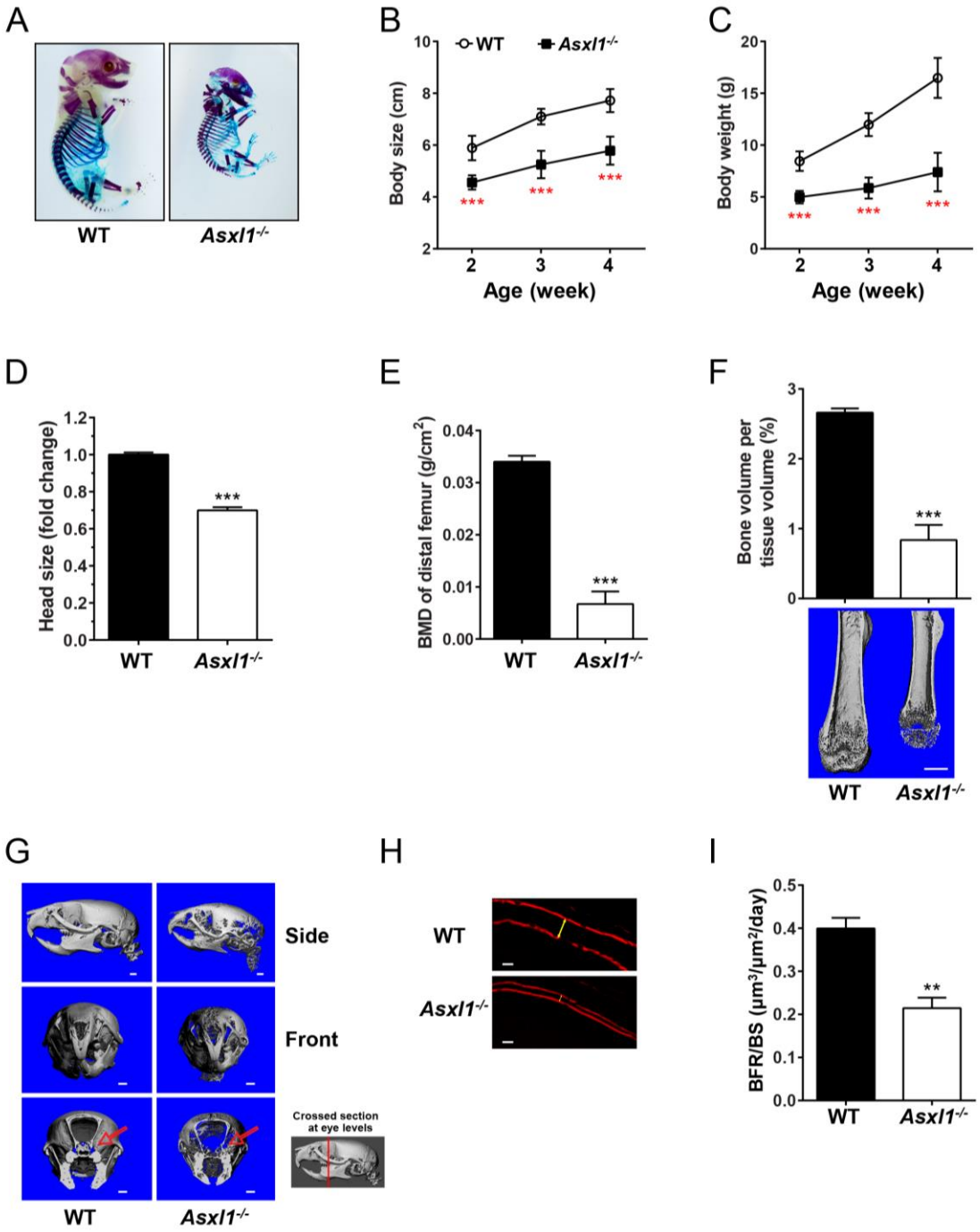

Figure S2. Related to Figure 3. (A) Whole-mount skeletal staining on embryonic day 18.5 shows reduced body size and characteristic eye defects in *Asxl1*$^{-/-}$ embryos compared with WT. (B-C) Serial measurements of body length (B) and weight (C) in WT and *Asxl1*$^{-/-}$ mice (n=12 mice per genotype) are shown. Mice were measured and weighed weekly at the same time. (D) Head size of *Asxl1*$^{-/-}$ mice, measured via X-ray images, is significantly smaller than WT mice (WT, n=12 mice; *Asxl1*$^{-/-}$ n=9 mice). (E) BMD of the distal femur was determined by pDEXA 3

weeks after birth. The *Asxl1*$^{-/-}$ mice exhibit significantly reduced BMD compared with WT littermates (n=14 mice per genotype). (F) µCT analysis of femurs from 3-week-old *Asxl1*$^{-/-}$ mice and WT littermates (n=5 mice per genotype). Bone volume is significantly decreased in *Asxl1*$^{-/-}$ mice. Representative µCT reconstructed femurs are shown for WT versus *Asxl1*$^{-/-}$ mice. Scale bar represents 1 mm. (G) Developmental abnormalities of the *Asxl1*$^{-/-}$ skull (upper) and eye (lower) are shown in representative µCT scans. Scale bar represents 1 mm. (H-I) Dynamic bone histomorphometry was preformed using alizarin labelling (H). The bone formation rate (BFR/BS, I) was significantly decreased in *Asxl1*$^{-/-}$ mice compared with WT littermates (n=3 mice per genotype). Scale bars represent 20 µm.

Data are presented as mean ± SEM. **$p < 0.005$, ***$p < 0.001$.

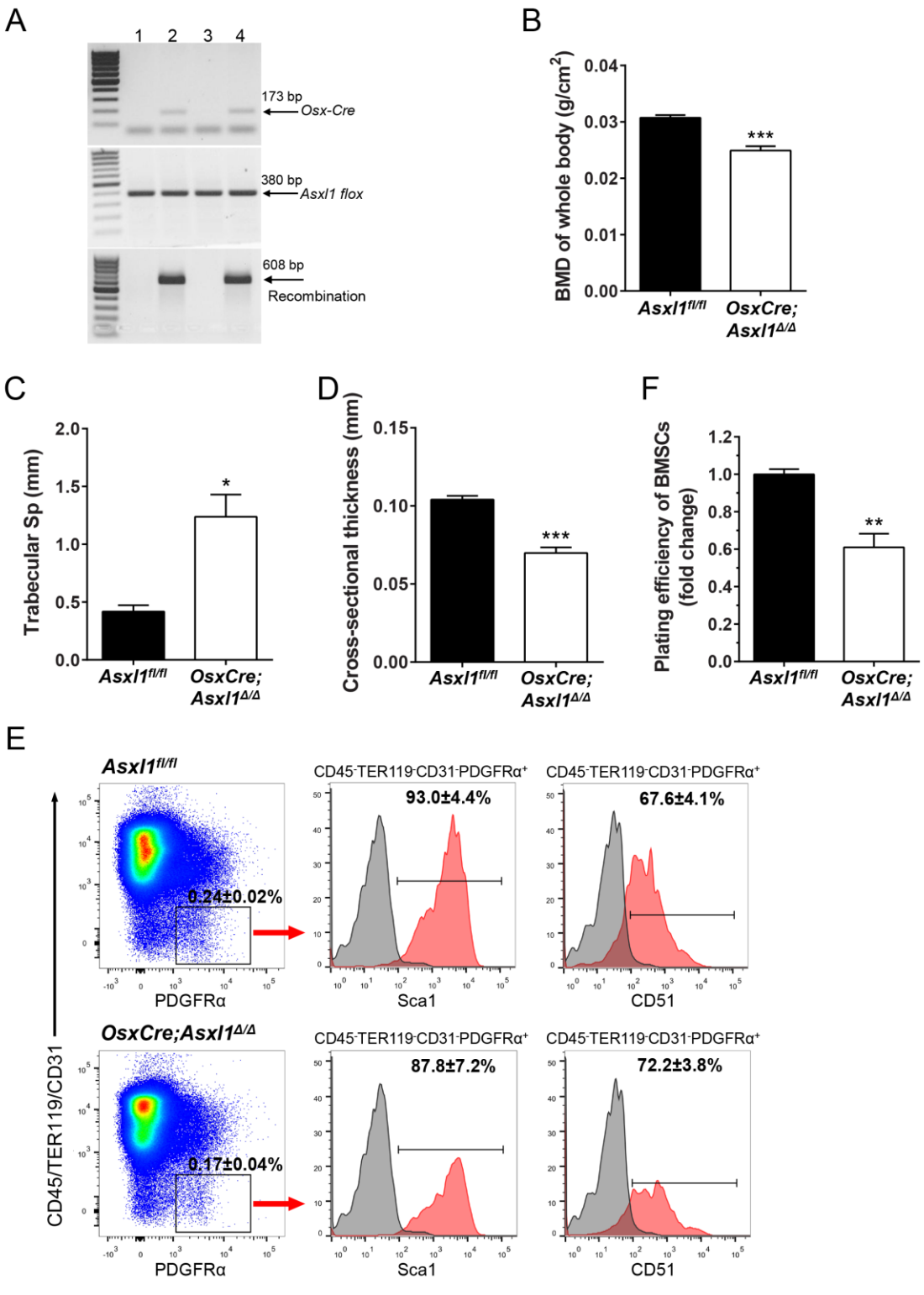

Figure S3. Related to Figure 3. (A) PCR genotyping of *OsxCre;Asxl1*$^{\Delta/\Delta}$ mice and *Asxl1*$^{fl/fl}$ littermates. DNA templates used for PCR analysis were obtained from mouse toes. Bottom PCR

shows the presence of a recombination band in *OsxCre;Asxl1*$^{\Delta/\Delta}$ mice, but not in *Asxl1*$^{fl/fl}$ littermates. (B) Whole body BMD of *OsxCre;Asxl1*$^{\Delta/\Delta}$ (n=6 mice) is significantly reduced compared with controls (n=4 mice). (C) µCT analysis of trabecular spacing in the femurs of *OsxCre;Asxl1*$^{\Delta/\Delta}$ (n=6 mice) and *Asxl1*$^{fl/fl}$ littermates (n=4 mice). (D) Cross-sectional cortical bone thickness of the femur midshaft is significantly decreased in *OsxCre;Asxl1*$^{\Delta/\Delta}$ (n=6 mice) compared with *Asxl1*$^{fl/fl}$ littermates (n=4 mice). (E) Representative flow cytometry plots show the population of PDGDRα^{+} BMSCs and the marker expression in the bone marrow of *OsxCre;Asxl1*$^{\Delta/\Delta}$ mice and littermate controls. n=4-6 mice from three independent experiments. (F) Plating efficiency of BMSCs from *OsxCre;Asxl1*$^{\Delta/\Delta}$ mice and *Asxl1*$^{fl/fl}$ littermates (n=4 mice per genotype).

Data are presented as mean ± SEM. *$p < 0.05$, **$p < 0.005$, ***$p < 0.001$.

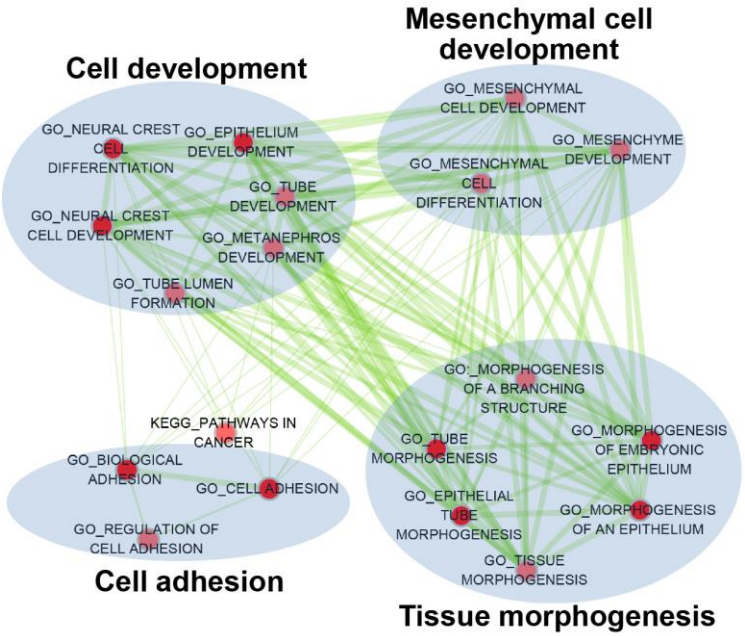

Figure S4. Related to Figure 4. Enrichment map was used for visualizing the network of KEGG pathways and GO terms enriched with up-regulated genes in *Asxl1*$^{-/-}$ BMSCs. Nodes and ovals indicate enriched functional gene sets ($p < 0.01$ and FDR < 0.25 in DAVID) and functional clusters, respectively. Edges indicate overlap between the enriched gene-sets; thickness represents significance. Only edges with a Fisher's exact test nominal p value smaller than 10^{-4} were visualized. Color intensity is proportional to enrichment significance.

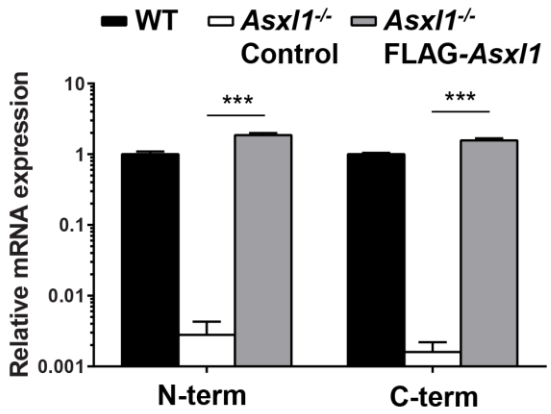

Figure S5. Related to Figure 5. qPCR shows the expression level of *Asxl1* mRNA in *Asxl1*$^{-/-}$ BMSCs rescued by transduction of FLAG-*Asxl1* from five independent experiments. N-term and C-term indicate the position of primers used.

Data are presented as mean ± SEM. ***$p < 0.001$.

Table S1. Primers used for qPCR.

Primer name	Primer Sequence (5'-3')	Product (bp)	Reference
Asxl1-F1 (N-term)	TCTACAGAGTCTCAGAGCCG	98	
Asxl1-R1 (N-term)	AGCATAACCCCAGTCCTTTTC		
Asxl1-F2 (C-term)	TCACACCGAAAAGCCACAG	120	
Asxl1-R2 (C-term)	GGGCATATCTGGTAAGTGGG		
Nanog-F1	AGGGTCTGCTACTGAGATGCTCTG	364	(Chen et al., 2006)
Nanog-R1	CAACCACTGGTTTTTCTGCCACCG		
Pou5f1-F1	CTGTAGGGAGGGCTTCGGGCACTT	485	(Chen et al., 2006)
Pou5f1-R1	CTGAGGGCCAGGCAGGAGCACGAG		
Sox2-F	ACAAGAGAATTGGGAGGGGT	120	
Sox2-R	TTTTCTAGTCGGCATCACCG		
Actb-F	GGCTGTATTCCCCTCCATCG	154	
Actb-R	CCAGTTGGTAACAATGCCATGT		
Runx2-F	ACACCGTGTCAGCAAAGC	99	
Runx2-R	GCTCACGTCGCTCATCTTG		
Bglap1-F	GGTAGTGAACAGACTCCGGC	96	
Bglap1-R	CAAGCAGGGTTAAGCTCACA		
Sp7-F	GATGGCGTCCTCTCTGCTT	146	
Sp7-R	CGTATGGCTTCTTTGTGCCT		
Alpl-F	ACTGCGCTCCTTAGGGCT	104	
Alpl-R	GGCAGCGTCAGATGTTAATTG		
Pparγ-F	GATGCACTGCCTATGAGCAC	110	
Pparγ-R	TCTTCCATCACGGAGAGGTC		
Cebpα-F	CCAAGAAGTCGGTGGACAAG	95	
Cebpα-R	TTGTTTGGCTTTATCTCGGC		
Fabp4-F	AATGTGTGATGCCTTTGTGG	100	
Fabp4-R	CACTTTCCTTGTGGCAAAGC		
Lpl-F	TTTGGCTCCAGAGTTTGACC	110	
Lpl-R	TGTGTCTTCAGGGGTCCTTAG		

Table S2. Antibodies used for western blot.

Antibodies	Catalogue Number
NANOG	Cell Signaling 8600
OCT4 (N-19)	Santa Cruz sc-8628
SOX2	Abcam ab59776
β-ACTIN	Sigma A2228
M2-FLAG	Sigma F3165

Supplemental Experimental Procedures

Chemicals were obtained from Sigma (St. Louis, MO) unless otherwise indicated.

ASXL1 Murine Models

The generation of *Asxl1:nlacZ/nGFP* knock-in and *Asxl1*$^{fl/fl}$ mice has been previously described (Abdel-Wahab et al., 2013; Wang et al., 2014). Heterozygous *Asxl1:nlacZ/nGFP* (*Asxl1*$^{+/-}$) mice were interbred to obtain homozygous *Asxl1:nlacZ/nGFP* (*Asxl1*$^{-/-}$) mice. *Osx-Cre* transgenic mice were purchased from Jackson Laboratories. All mice were bred on a C57BL/6 genetic background. All protocols were approved by the Institutional Animal Care and Use Committee at University of Miami Miller School of Medicine.

X-Ray, Peripheral Dual-Energy X-Ray Absorptiometry (pDEXA), and Micro-Computed Tomography (µCT)

The mice were anesthetized with ketamine (150 mg/kg) administered by intraperitoneal (IP) injection and placed in the lateral position in an XPERT 80 Digital Cabinet X-ray System (Kubtec, Milford, CT). Radiographs were acquired to demonstrate the size difference between WT and *Asxl1*$^{-/-}$ mice.

Bone mineral density (BMD) was measured by pDEXA with a Lunar Piximus densitometer (GE Medical Systems, software version 1.4 Lunar) (Yang et al., 2006). The mice were anesthetized and placed into the scanner in the prone position with arms and legs extended. The head was excluded from total body scans. The BMD of the left femoral metaphysis was measured by defining a region of interest of 12 pixels x 12 pixels proximal to the distal growth plate, a region containing a high content of trabecular bone.

Bone volume and microarchitecture in the distal femoral metaphysis were evaluated using a high-resolution desktop µCT imaging system (VivaCT 40; Scanco Medical AG, Basserdorf, Switzerland) (Rhodes et al., 2013). Scanning for the femur was started at 15% of the total femur length measured from the tip of femoral condyle and extending proximally for 200 slices with an increment of 9 µm, which were then reconstructed, filtered (σ=0.8 and support=1.0), and thresholded (at 16% of the possible gray scale value) for analysis (Munugalavadla et al., 2008). The area for trabecular analysis was outlined within the trabecular compartment, excluding the cortical and subcortical bone. Every 10 sections were outlined manually, and the intermediate sections were interpolated with the contouring algorithm to create a volume of interest.

Parameters of microarchitecture for both skeletal sites included bone volume (BV, mm^3), bone volume fraction (BV/TV, %), trabecular number (Tb.N, mm^{-1}), trabecular thickness (Tb.Th, mm), and trabecular spacing (Tb.Sp, mm).

Fluorochrome Bone Labeling

Fluorochrome labeling of the bones was performed in 3-week old mice by intraperitoneal injections of alizarin (20 mg/kg, Sigma) 8 and 3 days before sacrifice, as previously described (Warden et al., 2005; Wu et al., 2011). After sacrifice, femurs were fixed in 10% neutral buffered formalin for 48 hours, dehydrated in graded ethanols, and embedded undecalcified in methylmethacrylate.

Frontal sections (4 mm thick) were cut from the distal femur using a motorized microtome equipped with a tungsten-carbide knife (Leica Inc, Deerfield IL). The sections were mounted unstained for fluorochrome-derived bone formation parameters. Trabecular bone turnover was assessed by measuring the extent of single label (sL.Pm), double label (dL.Pm) and the area of bone (dL.Ar) between double alizarin labels using Image Pro Plus version 4.1 software (MediaCybernetics, Silver Spring, MD). Derived histomorphometric parameters included mineralizing surface (MS/BS, %), a measure of active bone-forming surface, calculated as follows: the [KsL.Pm+dL.Pm]/Tt.Pm * 100; mineral apposition rate (MAR, μm/day), a measure of the rate of radial expansion of new bone, calculated as follows: dL.Ar/dL.Pm/4 dy; and bone formation rate, an overall measure of bone formation that combines MS/BS and MAR, calculated as follows: MS/BS * MAR.

Flow Cytometry

Bone marrow stromal cell (BMSC) populations were delineated *in vivo* by evaluating the expression of surface markers by flow cytometry on a FACSCalibur. Antibodies for flow cytometry were purchased from BD-Pharmingen and BioLegend. BMSCs were stained with antibodies against CD146 (PE), CD105 (APC), CD45 (PerCP), CD44 (PE-Cy7), CD90 (APC-Cy7), and CD73 (PacBlue), or antibodies against PDGFRα (APC), CD51 (PE), Sca1 (PE-Cy7), CD45 (FITC), TER119 (FITC), and CD31 (FITC). Following incubation of cells with antibodies for 30 minutes at 4°C, cells were washed 3 times with PBS containing 0.1% bovine serum albumin (BSA) and analyzed using a FACSCalibur instrument (Becton Dickinson).

BMSC Culture and Lineage Differentiation Assays

To measure the frequency of BMSCs in bone marrow, the colony forming unit fibroblast (CFU-F) assay was performed as previously described (Wu et al., 2006). Briefly, $4x10^6$ of bone marrow mononuclear cells (BMMNCs) were plated into 6-well tissue culture plates in triplicate for each condition in mouse MesenCult medium (MesenCult basal media plus 20% of MesenCult Supplemental, Stem Cell Technologies Inc,) and incubated at 37°C and 5% CO_2. After 14 days of culture, medium was removed and each well was washed with phosphate-buffered saline (PBS), stained with a HEMA-3 quick staining kit (Fisher Scientific Company, VA, USA) according to the manufacturer's instructions and photographed.

For CFU-osteoblast assays, after 7 days of culture, medium was removed and switched to osteogenic differentiation medium (MesenCult medium supplemented with 10^{-7} M dexamethasone, 50 μg/mL ascorbic acid and 10 mM β-glycerophosphate). Medium was changed every other day for one week of continuous culture. Staining for ALP activity was subsequently performed using a Leukocyte Alkaline Phosphatase kit according to the manufacturer's instructions. Photomicrographs of the stained cells were acquired with a Nikon TE2000-S microscope. The area and intensity of ALP^+ cells were quantified using Image J software.

For CFU-adipocyte assays, after 5 days of culture, medium was changed to adipogenic differentiation medium (MesenCult medium supplemented with 10^{-7} M dexamethasone, 450 μM isobutylmethylxanthine, 1 μg/ mL insulin and 200 μM indomethacin). Culture medium was changed every 5 days for 4 weeks. Adipocytes were determined with Oil Red O staining.

BMSCs were generated from each experimental group of mice as previously described (Wu et al., 2006). Briefly, BMMNCs were separated by low density gradient centrifugation from 3- to 4-week old mice, and then resuspended and cultured in mouse MesenCult medium at 37°C and 5% CO_2. When the cultures reached 80 to 90% confluency, cells were trypsinized and replated. BMSCs of identical passage number (between passages 3 to 5) were used for experiments.

For osteoblast differentiation, $5x10^4$ BMSCs were cultured for 7 days in 6-well plates using osteogenic differentiation medium. To induce adipocyte differentiation *in vitro*, $1x10^5$ BMSCs were plated in 6-well tissue culture plates and cultured with adipogenic differentiation medium. For chondrocyte differentiation assays, $1x10^5$ BMSCs were plated in 6-well plates and cultured with chondrogenic differentiation medium (osteogenic differentiation medium supplemented with 10 ng/mL TGFβ3).

Mesensphere Assays

For clonal mesensphere formation, BMSCs were plated at clonal density (~1,000 cells cm^2) in ultralow adherent 24-well plates (Corning) as previously described (Mendez-Ferrer et al., 2010; Pinho et al., 2013). The growth medium contained 15% chicken embryo extract (Fisher Scientific), 0.1 mM β-mercaptoethanol, 1% non-essential amino acids, 1% N2 and 2% B27 supplements (Gibco), fibroblast growth factor (FGF)-basic, insulin-like growth factor-1 (IGF-1), epidermal growth factor (EGF), platelet-derived growth factor (PDGF) and oncostatin M (OSM) (Peprotech) (20 ng/mL) in DMEM/F12 (1:1)/human endothelial (Gibco) (1:2). The cultures were maintained at 37°C in a 5% CO_2, water-jacketed incubator and left untouched for 1 week to prevent cell aggregation in low density cultures. Half of the medium was changed weekly. The mesensphere colonies were detached with trypsin, and the cells were mechanically dispersed and re-plated back into ultralow adherent plates with culture medium. Secondary mesenspheres were counted after 7 days in culture.

Proliferation Assays

Cell proliferation was examined by the [^{3}H] thymidine incorporation assay as previously described (Wu et al., 2006). Briefly, $5x10^3$ WT or *Asxl1*$^{-/-}$ BMSCs were plated in 96-well flat-bottom plates in 100 μL MesenCult medium in a 37°C and 5% CO_2, humidified incubator overnight. The cells were starved with 100 μL α-MEM medium (Gibco) without supplements for 24 hours, and then cultured in MesenCult medium for 24 hours, and [^{3}H] thymidine was added to cultures 6 hours before harvest with an automated 96-well cell harvester (Brandel, Gaithersburg, MD). γ-Emission was measured with a microplate scintillation counter (PerkinElmer Life and Analytical Sciences, Boston, MA). Assays were performed in triplicate.

Generation of Stably *Asxl1*-Transduced BMSCs

The full-length mouse *Asxl1* cDNA with an N-terminal FLAG tag was cloned, and then subcloned into the lentiviral vector with *Xho*I and *Nhe*I double digestion and ligation. The empty vector was used for control. All constructs were validated by direct sequencing prior to lentiviral generation. Recombinant lentiviral vectors were produced in HEK293T cells using the helper plasmid pCD/NL-BH and the VSV-G envelope plasmid. Lentivirus containing supernatants were concentrated and tittered. BMSCs were split approximately 16 hours prior to transduction and

then transduced overnight with concentrated supernatants resuspended in MesenCult medium. Medium was replaced the next day and transduced cells were cultured and expanded. $EGFP^+$ cells were sorted using a FACS Vantage flow cytometer. Before further experiments, transduction and selection efficiency were verified by qPCR and western blot analysis.

Gene Expression Analysis by qPCR and RNA-Seq

Genes of interest mRNA levels were determined by real-time qPCR. Total RNA was extracted with TRIzol reagent (Ambion). qPCR was performed in triplicate using an ABI 7500 with SYBR green PCR kits (Applied Biosystems). mRNA levels were normalized to housekeeping gene *β-actin* expression. All qPCR primers used are listed in Table S1.

For RNA-seq, mRNA library preparation was performed with the Illumina TruSeq strand specific mRNA sample preparation system (Illumina). Briefly, mRNA was extracted from total RNA using polyA selection, followed by RNA fragmentation. A strand specific library was constructed by first-strand cDNA synthesis using random primers, sample cleanup and second-strand synthesis using DNA polymerase I and RNase H. A single 'A' base was added to the cDNA fragments followed by ligation of the adapters. A final cDNA library was achieved by further purification and enrichment with PCR, with quality checked using the Agilent 2100 Bioanalyzer. The library was sequenced (PE100bp) using the Illumina HiSeq2500, with 4 samples per lane, and final of over 20 million reads per sample.

RNA-seq reads were aligned to the mouse genome reference sequence (GRCm38/mm10) using TopHat (Trapnell et al., 2012) with a tolerance of two mismatches. Cuffdiff (Trapnell et al., 2012) was used to detect the differentially expressed genes with cutoff of $p < 0.05$ and false discovery rate (FDR) < 0.25. The identified differentially expressed genes were used for pathway enrichment analysis and functional annotation with the Database for Annotation, Visualization and Integrated Discovery (DAVID) Bioinformatics resources (Huang da et al., 2009). A heatmap was generated in R using the gplot package. GSEA analysis (Subramanian et al., 2005) was performed in MSigDB (http://www.broadinstitute.org/gsea/msigdb/index.jsp) to generate the list of the most differentially expressed genes, including Kyoto Encyclopedia of Genes and Genomes (KEGG) pathway signatures and stem cell signatures. Enriched gene sets were selected using a cut-off of $p < 0.05$ and FDR < 0.25 (Isserlin et al., 2014).

Western Blot Analysis

BMSC cell lysates were subjected to western blot analysis. Isolated proteins were fractionated using NuPAGE 4-12% Bis-Tris Gels (Invitrogen) and electro-transferred to PVDF membranes (Roche). Immunoblots were performed using specific antibodies (Table S2). After incubation with anti-rabbit IgG or anti-mouse IgG (GE Healthcare) antibodies conjugated with HRP, signals were detected using ECL chemiluminescence substrate (Pierce).

Statistical Analysis

Differences between experimental groups were determined by Student's *t*-test or ANOVA followed by Newman-Keuls multiple comparison tests as appropriate. p values of less than 0.05 were considered significant.

Supplemental References

Chen, S., Do, J.T., Zhang, Q., Yao, S., Yan, F., Peters, E.C., Scholer, H.R., Schultz, P.G., and Ding, S. (2006). Self-renewal of embryonic stem cells by a small molecule. Proceedings of the National Academy of Sciences of the United States of America *103*, 17266-17271.

Munugalavadla, V., Vemula, S., Sims, E.C., Krishnan, S., Chen, S., Yan, J., Li, H., Niziolek, P.J., Takemoto, C., Robling, A.G., *et al.* (2008). The p85alpha subunit of class IA phosphatidylinositol 3-kinase regulates the expression of multiple genes involved in osteoclast maturation and migration. Molecular and cellular biology *28*, 7182-7198.

Rhodes, S.D., Wu, X., He, Y., Chen, S., Yang, H., Staser, K.W., Wang, J., Zhang, P., Jiang, C., Yokota, H., *et al.* (2013). Hyperactive transforming growth factor-beta1 signaling potentiates skeletal defects in a neurofibromatosis type 1 mouse model. Journal of bone and mineral research : the official journal of the American Society for Bone and Mineral Research *28*, 2476-2489.

Yang, F.C., Chen, S., Robling, A.G., Yu, X., Nebesio, T.D., Yan, J., Morgan, T., Li, X., Yuan, J., Hock, J., *et al.* (2006). Hyperactivation of p21ras and PI3K cooperate to alter murine and human neurofibromatosis type 1-haploinsufficient osteoclast functions. The Journal of clinical investigation *116*, 2880-2891.